SUPERALLOYS II

Edited by

CHESTER T. SIMS
Rensselaer Polytechnic Institute
Troy, New York

NORMAN S. STOLOFF
Rensselaer Polytechnic Institute
Troy, New York

WILLIAM C. HAGEL
Arbormet Ltd.
Ann Arbor, Michigan

A Wiley-Interscience Publication
JOHN WILEY & SONS
New York • Chichester • Brisbane • Toronto • Singapore

Library of Congress Cataloging in Publication Data:

Superalloys II.

"A Wiley-Interscience publication."
Includes bibliographies.
1. Heat resistant alloys. I. Sims, Chester T. (Chester Thomas), 1923– II. Stoloff, N. S. III. Hagel, William C. IV. Title: Superalloys II.

TN700.S85 1987 671 86-32564
ISBN 0-471-01147-9

Printed in the United States of America

10 9 8 7 6 5 4 3 2 1

Chapter 11

High-Temperature Oxidation

JAMES L. SMIALEK and GERALD H. MEIER

NASA Lewis Research Center, Cleveland, Ohio,
and University of Pittsburgh, Pittsburgh, Pennsylvania

Resistance to oxidizing environments at high temperatures is a requisite for superalloys whether used coated or uncoated. Therefore, an understanding of superalloy oxidation and how it is influenced by alloy characteristics and exposure conditions is essential for effective design and application of superalloys. In this chapter a brief review of the fundamentals of the oxidation of metals and alloys is presented, followed by a discussion of simple Cr_2O_3- and Al_2O_3-forming alloys. The effects of common alloying elements on the oxidation behavior of these base systems are then discussed, which provides the basis for a broad treatment of the oxidation behavior of complex superalloys.

FUNDAMENTAL PRINCIPLES OF ALLOY OXIDATION

The major aspects of the oxidation of metals and alloys will be briefly reviewed in this section.

Pure Metals

The diffusion-controlled growth rate of an oxide layer of thickness x is observed usually to follow the equation

$$dx/dt = \frac{k'}{x} \tag{1}$$

where k' is called the "parabolic rate constant" with units cm^2/sec. The integrated form of this equation is

$$x_t^2 - x_{t_0}^2 = 2k'(t - t_0) \tag{2}$$

where t_0 is the time at which diffusion control begins. The extent of reaction may also be expressed in terms of mass change per unit area, $\Delta m/A$, according to

$$\left(\frac{\Delta m}{A}\right)_t^2 - \left(\frac{\Delta m}{A}\right)_{t_0}^2 = 2k''(t - t_0) \tag{3}$$

where

$$k'' = \left(\frac{8}{V}\right)^2 k' \tag{4}$$

and V is the equivalent volume of the oxide. The units of k'' are g^2/cm^{-4}. (See Chapter 3 of Birks and Meier[1] for a discussion of units and conversions.)

Wagner[2] provided a theoretical treatment for k' based on the following assumptions:

1. The oxide layer is a compact, perfectly adherent scale.
2. Migration of ions or electrons across the scale is the rate-controlling process.
3. Thermodynamic equilibrium is established at both the metal–oxide and oxide–gas interface.
4. The oxide shows only small deviations from stoichiometry.
5. Thermodynamic equilibrium is established locally throughout the scale.
6. The scale is thick compared with the distances over which space charge effects occur.
7. Oxygen solubility in the metal may be neglected.

The results of this treatment may be expressed by the following expression:

$$k' = \frac{1}{RT} \int_{\mu_O'}^{\mu_O''} \left(D_O + \frac{Z_M D_M}{2}\right) d\mu_O \tag{5}$$

where D_M and D_O are the diffusivities of M and O, respectively, in the oxide, and Z_M is the metal volume, and μ'_O and μ''_O are the chemical potentials of O at the metal–oxide and oxide–gas interfaces, respectively. Good agreement has been found between experimentally determined rate constants and those calculated from the Wagner theory for a number of metals reacting with oxygen, sulfur, and halogens.[3]

The majority of data, however, deviate from the Wagner model because one or more of Wagner's assumptions are not satisifed in the real systems. This is particularly true when assumption 2 is not satisfied, in which case the rate of scale growth will not follow a simple parabolic expression such as equations (2) or (3). Nevertheless, the use of parabolic rate constants is a convenient way to compare the relative rates of oxidation for the many cases that exhibit approximately parabolic behavior, as illustrated in Fig. 1.

Alloys

The oxidation of alloys is more complex than that of pure metals. Following Wagner[4] alloys may be grouped as (1) noble parent with alloying elements of a more base (less noble) nature and (2) base parent with base alloying elements. Typical oxidation morphologies within these two groups are presented in Figs. 2 and 3. A comprehensive treatment of the diffusion processes leading to these and other morphologies has been given by Whittle.[5] In Fig. 2 element A represents a noble parent (i.e., it will not react with oxygen at the ambient pO_2) and element B represents a base solute (i.e., the dissociation pressure of the oxide BO is less than the ambient pO_2). If B is present in dilute concentration and oxygen is soluble in A, a morphology such as Fig. 2a will result, in which BO precipitates internally. In the simplest case for which BO is very stable and $D_B << D_O$ in the alloy the depth of internal oxidation X may be written as

$$X(t) = \left(\frac{2N_O^{(s)} D_O t}{N_B^{(0)}}\right)^{1/2} \tag{6}$$

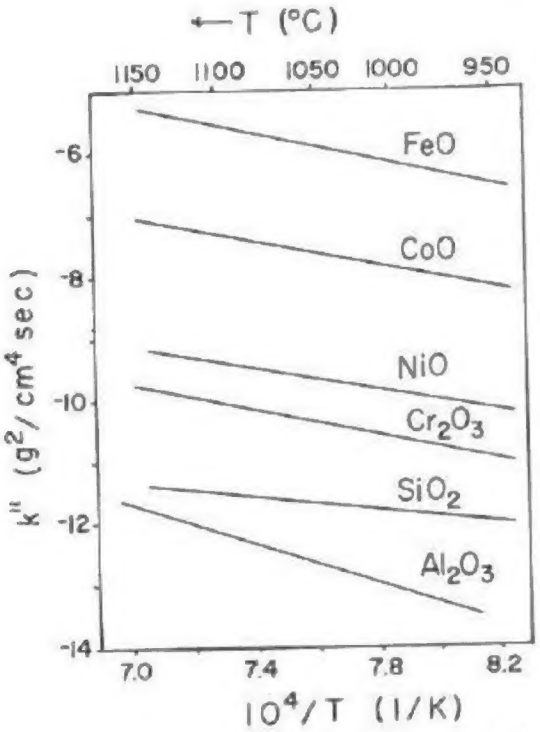

Fig. 1. Order-of-magnitude rate constants for the growth of selected oxides.

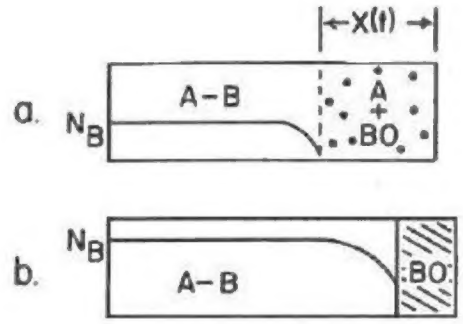

Fig. 2. Schematic cross sections and concentration profiles for oxidation of a noble metal, A, alloyed with a reactive metal, B. (a) Alloy dilute in B showing internal oxidation of B. (b) Alloy concentrated in B showing formation of an external layer of BO.

where $N_O^{(s)}$ is the oxygen solubility and $N_B^{(0)}$ is the bulk alloy concentration of B both expressed as atom fraction. Equation (6) indicates that $X(t)$ decreases as $N_B^{(0)}$ increases, and when sufficient B is present, the outward flux of B results in BO being formed as a continuous surface layer (Fig. 2b). This transition from internal to external oxidation occurs when $N_B^{(0)} > N_B^{(\text{critical})}$, where

$$N_B^{(\text{critical})} = \left(\frac{\pi g^*}{3} N_O^{(s)} \frac{D_O V_M}{D_B V_{ox}}\right)^{1/2} \tag{7}$$

where V_M and V_{ox} are the molar volumes of alloy and oxide, respectively, and g^* is the critical volume fraction of oxide required for the transition, which is often around 0.3.

Figure 3 presents the more general case where the oxides of both A and B are stable in the gas but BO is more stable than AO (in superalloys A generally represents Ni or Co and B represents Cr, Al, Ti, etc.). For low concentrations of B an external layer of AO will form, and internal oxides of BO will precipitate in the alloy (Fig. 3a). If the concentration of B is increased to exceed the critical concentration for transition to external oxidation, a morphology such as that in Fig. 3 develops. The

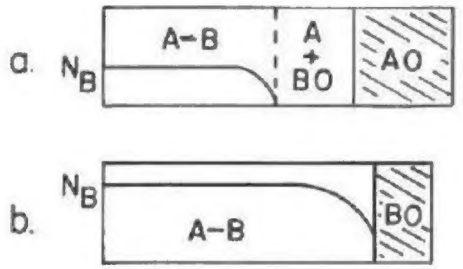

Fig. 3. Schematic cross sections of an A–B alloy where both components form stable oxides but BO is more stable than AO. (a) Alloy dilute in B showing internal oxidation of B under an external layer of AO. (b) Alloy concentrated in B showing continuous external BO.

formation of a continuous layer of BO precludes any further formation of the less stable AO, although some AO will generally form before the BO layer becomes continuous, that is, "transient oxidation." The morphology depicted in Figure 3b is the objective of alloying for oxidation resistance. That is, an alloying element B, which forms an oxide that is both very stable and slow growing, is added in sufficient quantity to form a protective surface layer by "selective oxidation."[6]

The oxidation rate of an alloy such as that in Fig. 3b will be essentially parabolic with a rate constant characteristic of BO. However, as seen from the concentration profile of B, selective oxidation depletes B from the alloy under the scale. This depletion will eventually result in an enrichment of oxides of A in the scale with the rate increasing toward that characteristic of AO. The length of time required for the transition to a more rapid rate will depend on a number of factors such as temperature, specimen size, diffusivities in the alloy and scale, and initial concentration of B in the alloy. The transition is hastened by any process that lessens the protectiveness of the BO layer. This can occur by evaporation of a volatile oxide species (e.g., CrO_3 from Cr_2O_3) that thins the protective layer or by mechanical damage to the scale by the action of erosive particles or cracking and spalling due to applied or generated stresses. The latter situation is particularly important since most superalloys undergo thermal cycling during service that is accompanied by stress generation due to thermal expansion mismatch between the oxide and alloy. The results of thermal cycling are shown schematically in Fig. 4, which compares the isothermal and cyclic oxidation weight changes of a given alloy. Initially the rate of weight gain in cyclic exposure is similar to the isothermal rate but eventually goes through a maximum and then decreases. This decrease, which is due to oxide spalling,

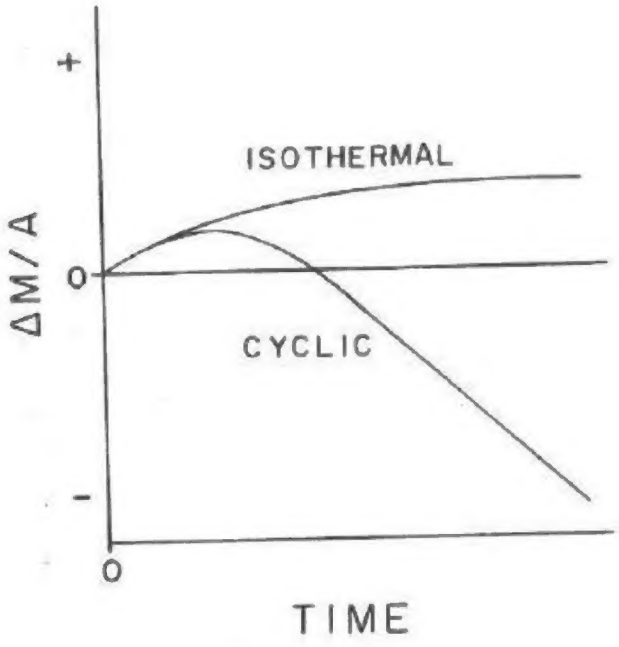

Fig. 4. Schematic plot of weight change vs. time comparing isothermal and cyclic oxidation behavior of the same alloy.

actually corresponds to a more rapid rate of consumption of the alloy. In many situations cyclic oxidation rates such as that in Fig. 4 may be approximated by

$$\frac{\Delta m}{A} = k_1^{1/2} t^{1/2} - k_2 t \tag{8}$$

where k_1 is a growth constant and k_2 a spalling constant.[7]

OXIDATION OF M–CR ALLOYS (CR_2O_3 FORMERS)

A large number of nickel-base superalloys and virtually all Co- and Fe-base superalloys rely on the formation of Cr_2O_3 scales for oxidation resistance. Therefore, the oxidation of binary alloys with chromium will be discussed here. The oxidation behavior of nickel–chromium alloys may be separated into three groups.[8] In Group I, which corresponds to dilute alloys (< 10% Cr), the oxidation morphologies are similar to Fig. 3a, that is, external NiO scales and internal Cr_2O_3 precipitates. For this group the rate constants are somewhat larger than those for pure nickel due to "doping" of the NiO scale with chromium, which results in an increased diffusivity of nickel ions. In Group III (≥30% Cr) the oxidation morphologies are similar to Fig. 3b, that is, external Cr_2O_3 scales. For this group the rate constants are several orders of magnitude smaller than those for pure nickel. In Group II external scales of Cr_2O_3 were observed over alloy grain boundaries, while external NiO scales formed over alloy grains with corresponding formation of internal Cr_2O_3. Concentrations of chromium of 30 wt. % or more are required for purely external Cr_2O_3 scales. The oxidation of cobalt–chromium and iron–chromium alloys are qualitatively similar to nickel–chromium. However, the rate constants for Cr_2O_3 growth on nickel-, cobalt-, and iron-base alloys vary by two orders of magnitude with no apparent correlation with substrate alloy.[9]

Growth of Cr_2O_3

The apparent variability of the rate constant for Cr_2O_3 growth on various substrates requires discussion of the defect structure and growth mechanism of Cr_2O_3. Kofstad and Lillerud[10] reviewed the existing literature on nonstoichiometry and concluded that the predominant defects in Cr_2O_3 at low pO_2 are chromium interstitials compensated by electrons and that at high pO_2, Cr_2O_3 is an intrinsic semiconductor. Seebeck coefficient measurements on sintered Cr_2O_3 also indicate chromium interstitials to be the predominant ionic defect at low pO_2.[11] However, the pO_2 dependence of the chromium diffusivity in single-crystal Cr_2O_3 (see ref. 12) and the deviation from stoichiometry in polycrystalline Cr_2O_3 (see ref. 13) are consistent with chromium vacancies being the predominant defect. However, these measurements are not necessarily contradictory since the highest pO_2 used indicating chromium interstitials in the Seebeck effect measurements was about four orders of magnitude lower than

the lowest pO_2 used in the diffusion measurements. Therefore, it is possible that the predominant ionic defects in Cr_2O_3 are chromium vacancies at high pO_2 and chromium intersitials at low pO_2, perhaps with a zone of intrinsic semiconduction separating the two regimes.

The above discussion of lattice defects in Cr_2O_3 cannot be applied, in most cases, to the growth of Cr_2O_3 on pure chromium or chromium-containing alloys since it has become clear that short-circuit diffusion predominates during this process. The rate constant for Cr_2O_3 growth calculated from equation (5) using the lattice diffusion coefficient for chromium in Cr_2O_3 is always many orders of magnitude smaller than the experimental value for the growth of polycrystalline Cr_2O_3.[12,14] Also in rare instances when single-crystal Cr_2O_3 scales form, the growth rate is orders of magnitude slower than for polycrystalline Cr_2O_3.[15] The single-crystal scales are uniform and planar, whereas the polycrystalline scales become buckled and detached from the substrate. These observations have led to the proposal that grain boundaries in the oxide provide the short-circuit paths for diffusion of cations and, perhaps, anions.[15] Indeed, grain-size-dependent growth rates for Cr_2O_3 have been observed.[16] Therefore, it appears likely that much of the variability of Cr_2O_3 growth rates is associated with the scale microstructure and the availability of short-circuit diffusion paths. However, a quantitative correlation between growth rate and detailed scale microstructure is still needed.

Effect of Oxygen-Active Elements and Oxide Dispersions

Small alloy additions of rare-earth elements and other oxygen-active elements have been found to alter the oxidation resistance of Cr_2O_3-forming alloys.[17–20] The effects of these additions usually include (1) formation of continuous Cr_2O_3 scales at lower alloy chromium concentrations, (2) reduction in the rate of Cr_2O_3 growth, (3) improved scale adhesion, (4) change in the primary growth mechanism of the oxide from outward cation migration to inward anion migration, and (5) a reduction of the grain size in the Cr_2O_3 scale. Similar effects have also been observed when the oxygen-active elements are present as a fine oxide dispersion in the alloy prior to oxidation.[21–25] The effects of cerium on reducing growth rates and increasing adherence of Cr_2O_3 scales are illustrated in Fig. 5.

These observations have been explained in terms of (1) dispersoid accumulating at the metal–oxide interface and eventually blocking diffusive transport,[21] (2) dispersoid particles acting as heterogeneous nucleation sites for oxide grains to reduce the internuclear distance and allowing more rapid formation of a continuous Cr_2O_3 film with finer grain size and fewer short-circuit paths for cations (probably dislocations) so that anion diffusion becomes rate controlling,[24] or (3) oxide particles of the oxygen-active element serving as nucleation sites to produce a fine-grained scale and the ions of these elements blocking grain boundary transport through the Cr_2O_3 scale.[20] Similar effects have been observed when CeO_2 powder was applied to the surface of a nickel–chromium alloy and ion implantation of elements such as ytrrium and cerium have been observed to decrease Cr_2O_3 growth on nickel–chromium[26] and iron–nickel–chromium[27] alloys.

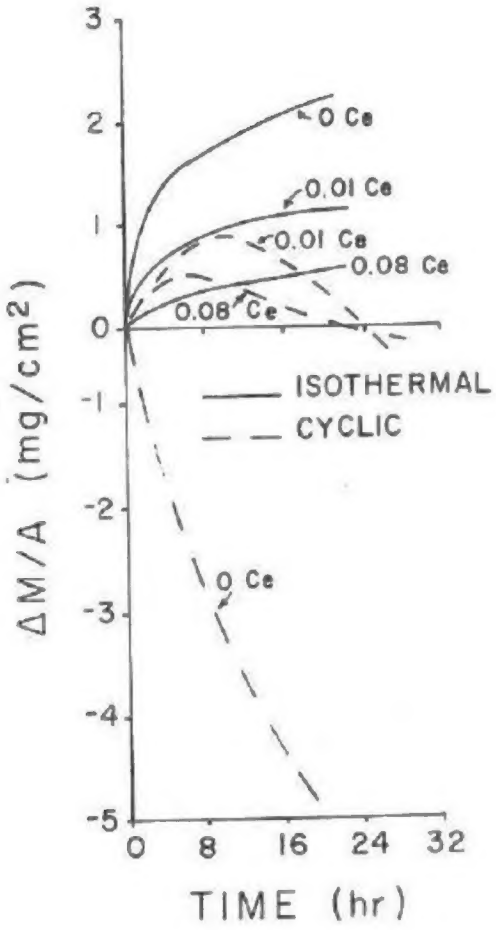

Fig. 5. Effect of Ce additions on the isothermal and cyclic oxidation behavior of Ni–50Cr (at. %) in O_2 at 1100 °C (2010 °F).[20]

Oxide Volatility Effects

Alloys that form protective Cr_2O_3 scales are susceptible to accelerated degradation at very high temperatures in high pO_2 gases due to the reaction

$$Cr_2O_3(s) + \frac{3}{2} O_2(g) = 2CrO_3(g) \tag{9}$$

The evaporation of CrO_3 results in the continuous thinning of the Cr_2O_3 scale so the diffusive transport through it is rapid. The effect of the volatilization on the oxidation kinetics have been analyzed.[28] The results for the oxidation of chromium are shown in Fig. 6. Initially, when the diffusion through a thin scale is rapid, the effect of CrO_3 volatilization is not significant, but as the scale thickens, the rate of volatilization becomes comparable and then equal to the rate of diffusive growth. This situation, paralinear oxidation, results in a limiting scale thickness, x_0, for which $dx/dt = 0$, as shown schematically in Fig. 6a. The occurrence of a limiting scale thickness implies protective behavior, but in fact, the amount of metal consumed increases until a constant rate is achieved. This can be seen more clearly by considering the metal recession (Fig. 6b). This problem is one of the major limitations on the

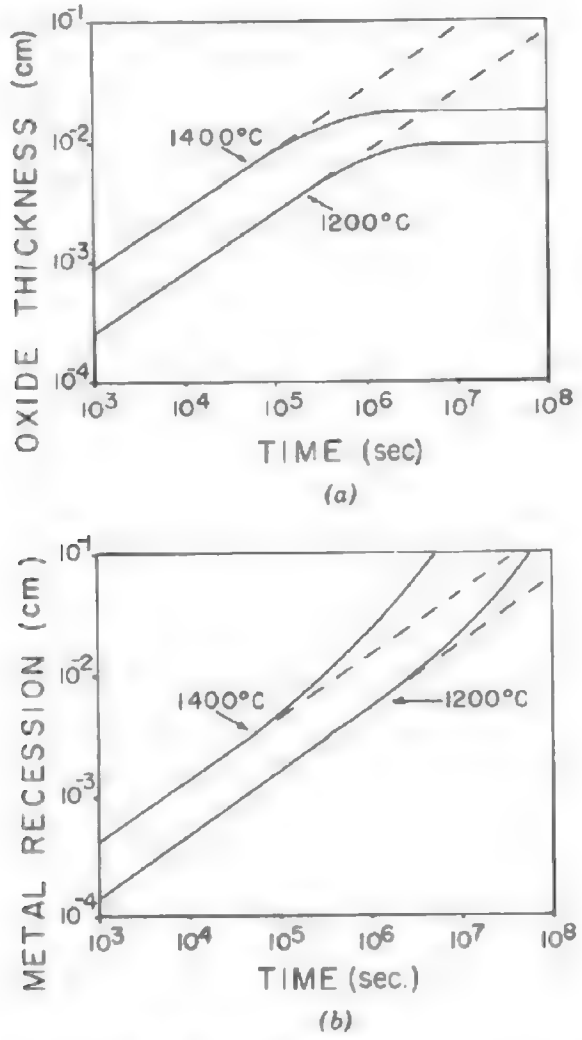

Fig. 6. Effect of CrO_3 evaporation on the oxidation behavior of Cr. (a) Oxide thickness reaches steady state with time. (b) Metal recession rate increases with time.[28]

very high-temperature use of Cr_2O_3-forming alloys and coatings. It becomes significant at temperatures around 1000 °C and even lower in the presence of high-velocity gases. In these situations Al_2O_3-forming alloys are more resistant since there are no vapor species in the aluminum–oxygen system with significant vapor pressures.

AL_2O_3-FORMING SYSTEMS; COATING ALLOYS

In addition to chromium, aluminum plays a critical role in the oxidation of γ'-strengthened superalloys. This element also provides the basis of oxidation-resistant NiAl diffusion aluminide and MCrAlY overlay coatings described in Chapter 13. This section is therefore concerned with the mechanism of exclusive Al_2O_3 growth and adhesion.

Effect of Aluminum Content

On the basis of thermodynamics alone, exclusive Al_2O_3 scales should be formed on nickel–aluminum alloys at levels as low as 1 ppm aluminum.[29] In actuality, the

process is kinetically limited by the opposing diffusional fluxes in the alloy of oxygen inward and aluminum outward. These promote nonprotective internal oxidation or protective external scales, respectively. Analogous to nickel–chromium oxidation, exclusive Al_2O_3 scales will be formed as opposed to discontinuous internal Al_2O_3 precipitates when the aluminum content is sufficiently high to produce the critical mole fraction of oxide particles required for particle link-up. Growth of external Al_2O_3 scales can be sustained when the flux of aluminum in the alloy exceeds that consumed by scale thickening:

$$J^{Al}_{alloy} > J^{Al}_{oxide} \tag{10}$$

The nickel–aluminum system is characterized by three regions shown in Fig. 7a: (I) 0–6% aluminum, internal $Al_2O_3(+NiAl_2O_4)$ oxides + NiO external scales result; (II) 6–17% aluminum, external Al_2O_3 forms initially, cannot be sustained due to an inadequate supply of aluminum and is overtaken by a fast growing $NiO+NiAl_2O_4+Al_2O_3$ oxide mixture; (III) $\geq$17% aluminum, the external Al_2O_3 scale is maintained due to a sufficient supply of aluminum. Higher temperature extends this region to lower aluminum contents.

Changes in oxidation kinetics go hand in hand with the scales formed (Fig. 7b). At low aluminum contents, k_p(NiO) is increased by approximately one order of magnitude due to Al^{3+}-doped NiO scales plus some internal oxidation. As more Al_2O_3 is formed (region II) k_p drops by one to two orders of magnitude. Lower growth rates are observed for higher temperatures because of the increased tendency for an exclusive Al_2O_3 scale. At 25% (region III), only Al_2O_3 is formed, and k_p is reduced by another one to three orders of magnitude.

Effects of Chromium Additions

Ni(Co,Fe) base alloys with *both* chromium and aluminum additions benefit from a remarkable synergistic effect of these elements amounting to great technological importance. For example, chromium additions of about 10 w/o can enable external Al_2O_3 scale formation on alloys having aluminum levels as low as 5 w/o. (This is in contrast to $\geq$17% Al for binary alloys.) This phenomenon has allowed for the design of more ductile and diffusionally stable MCrAl coatings as well as the matrix compositions for ODS alloys.

The compositional control of oxidation is most easily summarized in oxide maps of scale components and weight change as a function of chromium and aluminum content. In Fig. 8a three primary regions of oxidation can be seen corresponding to (I) NiO external scales + Al_2O_3/Cr_2O_3 subscales; (II) Cr_2O_3 external scale + Al_2O_3 subscales; and (III) external scales of only Al_2O_3. Long-duration cyclic oxidation has the effect of substantially contracting the region of optimum performance to higher aluminum and chromium contents (Fig. 8b). A wide transition zone forms in its place due to oxide spalling, accelerated aluminum removal, and the formation of $NiO+NiCr_2O_4+NiAl_2O_4+Al_2O_3$ composite scales.

The role of chromium in producing Al_2O_3 scales at much lower aluminum contents than in binary nickel–aluminum alloys can be described by the general

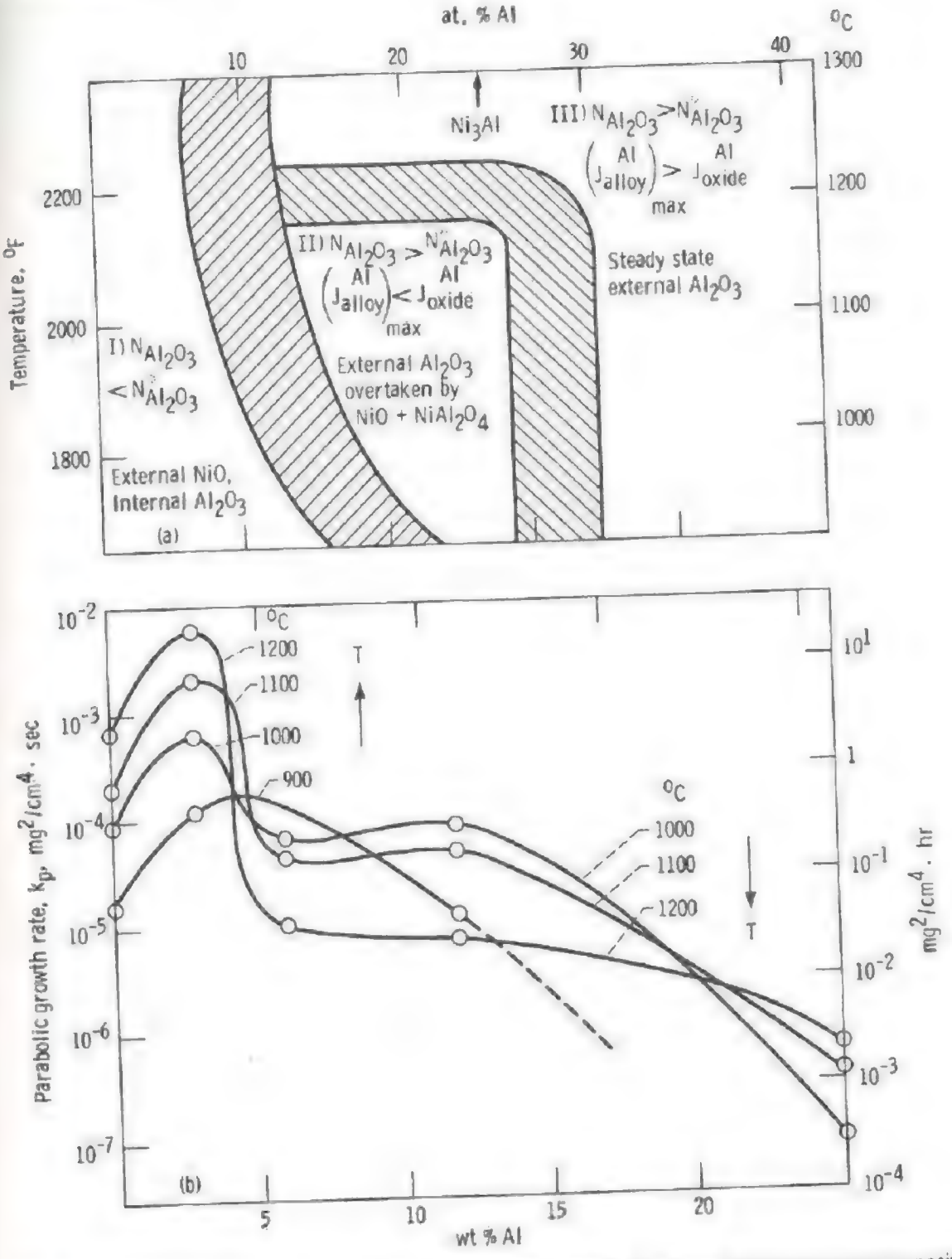

Fig. 7. Composional effects on the oxidation behavior of binary Ni – Al alloys. (a) Temperature-composition oxide phase map. (b) Scale growth rates corresponding to regimes in (a).[29]

oxidation phenomenon known as "gettering."[34] The mechanistic details of NiCrAl transient oxidation best illustrates this phenomenon[30,35] and is described for Ni–15Cr–6Al specifically in the schematic of Fig. 9.[35] The initial oxide (a) contains all the cations of the immediate alloy surface resulting in 15% NiO–85% $Ni(Cr,Al)_2O_4$ coverage (fast cation transport also causes some overgrowth of NiO); (b) subscale formation of Cr_2O_3 occurs because it is stable at the low oxygen activity defined

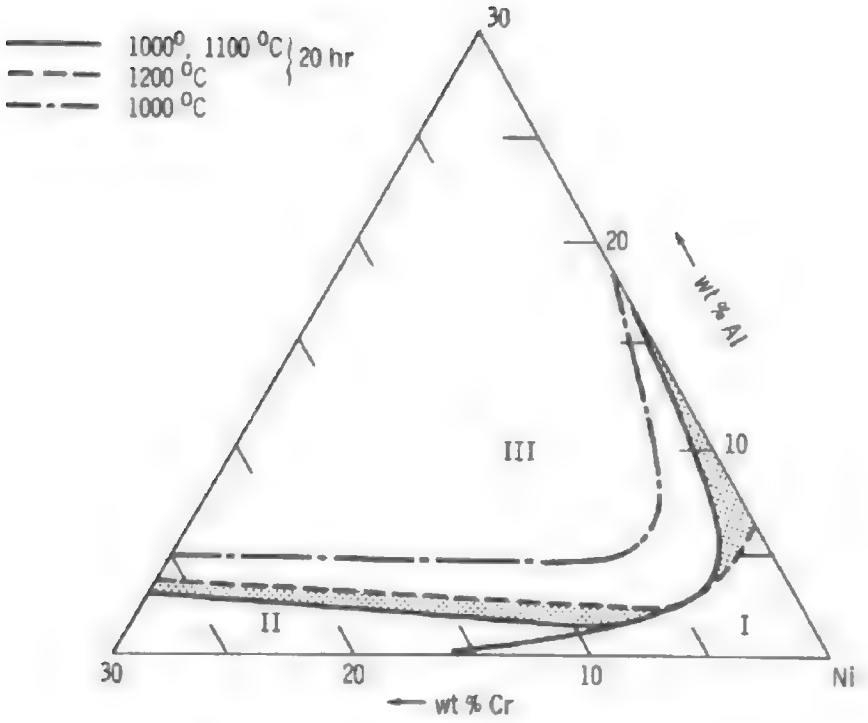

I External NiO, Internal $Cr_2O_3/Al_2O_3/Ni(Al, Cr)_2O_4$
II External Cr_2O_3, Internal Al_2O_3
III External Al_2O_3

(a) **Isothermal map.**

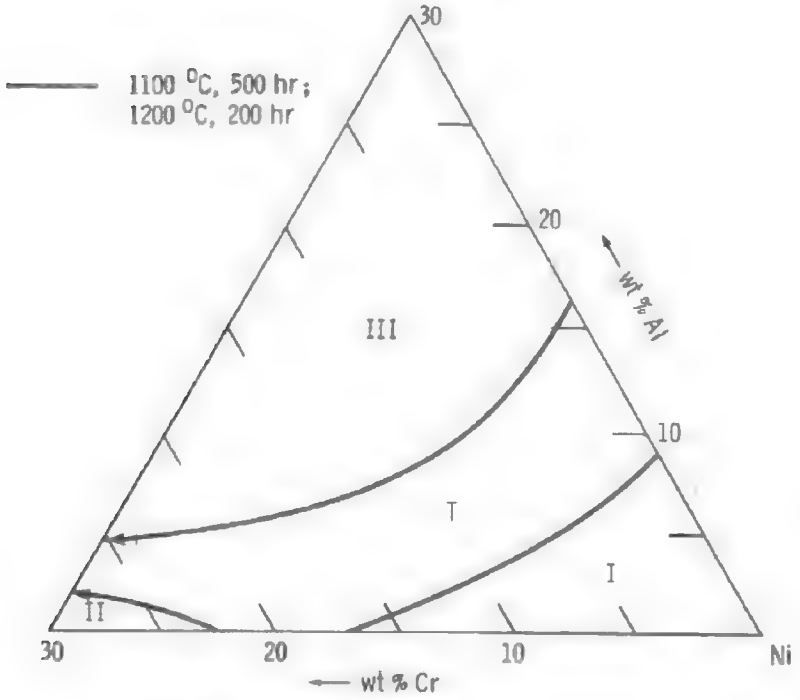

I Mostly NiO
II Mostly Cr_2O_3
III Al_2O_3(+$NiAl_2O_4$)
T NiO, $NiCr_2O_4$, $NiAl_2O_4$, Al_2O_3 Transition

(b) **Cyclic map.**

Fig. 8. Compositional effects on the oxidation behavior of Ni–Cr–Al ternary alloys.[30,31,32,33]

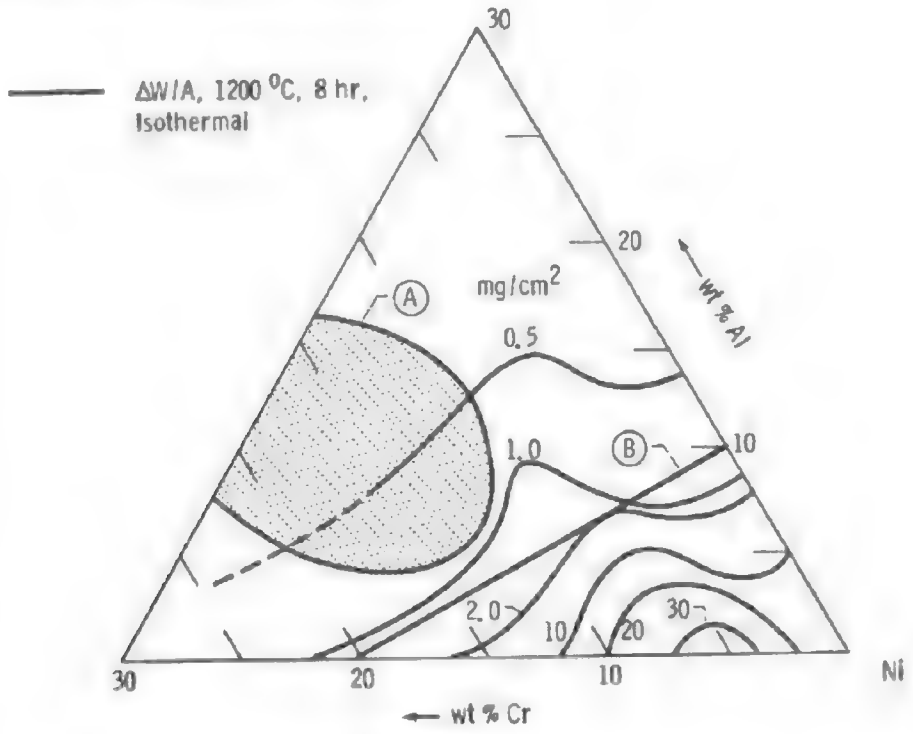

(c) **Weight change contour map.**

Fig. 8. (*Continued*)

by the NiO-alloy equilibrium, and internal oxidation of Al_2O_3 occurs ahead of this front since it is stable at the even lower activities here. The high chromium content results in a continuous Cr_2O_3 subscale (c) that defines a lower scale-alloy oxygen activity, reduces oxygen diffusion, and curtails internal Al_2O_3 formation. Further $NiO/Ni(Cr,Al)_2O_4$ growth is also blocked. Eventually, the Al_2O_3 subscale becomes continuous and rate controlling. Steady state is generally achieved in less than 1 h at 1000 °C. This cooperative action of chromium is also seen to have a very subtle nature: intimate mixtures of crystallographically coherent 0.1-μm subgrains of $Ni(Cr,Al)_2O_4$- and $(Cr,Al)_2O_3$-alloyed scales precede pure α-Al_2O_3 nucleation at the oxide–metal interface.[38]

Oxide growth rates can generally be grouped by the regions, and $k_p(\mathrm{I}) > k_p(\mathrm{II}) > k_p(\mathrm{III})$ by more than an order of magnitude for each grouping, as shown in Fig. 10.[30,36,37,39] This figure provides an interesting perspective on the comparison of pure nickel to Group I, Ni–30Cr to Group II, and Ni–25Al to Group III alloys. The three differentials caused by a ternary addition are the results of (1) aluminum- and chromium-doped NiO, (2) aluminum gettering assistance for Cr_2O_3 control, and (3) greater chromium doping of Al_2O_3 (for groups I, II, and III, respectively).

Somewhat more weight change detail can be seen from the contour map of Fig. 8c. Maximum oxidation resistance is suggested for compositions greater than 10%

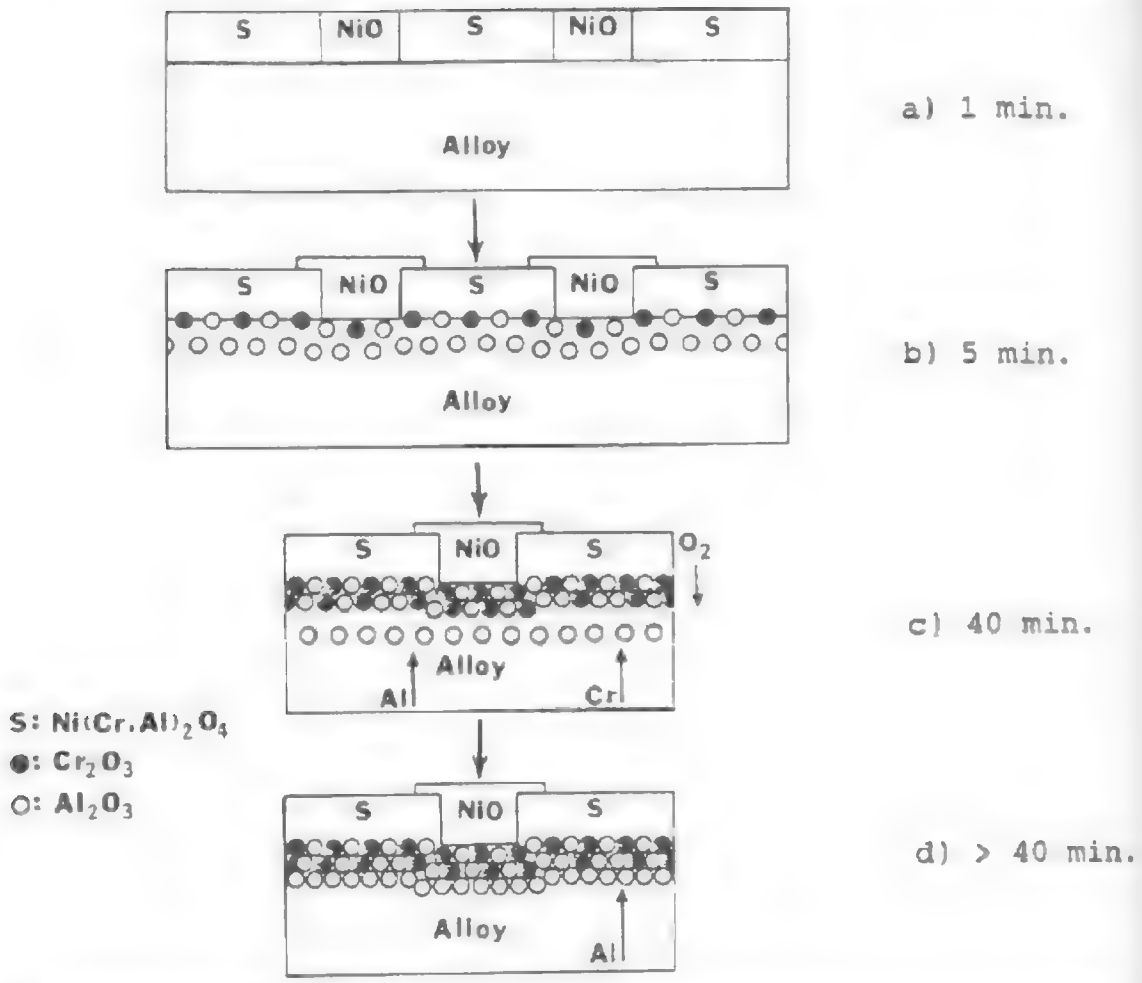

Fig. 9. Synergistic effect of Cr on the production of Al_2O_3 scales; gettering during transient oxidation of Ni–15Cr–6Al at 1000 °C (1830 °F): (a) 1 min; (b) 5 min; (c) 40 min; (d) >40 min (see text for discussion).[35]

chromium and 10% aluminum, that is, the region used for actual NiCrAl coatings. There is some indication that chromium additions under 10% are detrimental for all nickel–aluminum compositions, especially in long-term (100–500-h) or cyclic conditions.[32,33] This is in apparent disagreement with some studies[30,40] and would not be predicted on the basis of oxide phase maps alone (Figs. 8a,b). On the other hand, aluminum increases beyond 3–5 are always found to be beneficial to oxidation resistance (cf. Fig. 7).[29,32,33,39,40]

Effects of Oxygen-active Dopants: Mechanism of Al_2O_3 Scale Growth and Adhesion

Rare-earth or oxygen-active elements produce dramatic modifications to MCrAl oxidation behavior that are equal in importance to those arising from aluminum or chromium additions. Small amounts (<1%) of these dopant elements prevent the Al_2O_3 scales from otherwise spalling at the oxide–metal interface. Discussion of the adherence effect is usually entwined with diffusion, growth, and morphological phenomena, as presented below.

Diffusion in Al_2O_3. Oxygen diffusion in α-Al_2O_3 occurs predominantly by grain boundaries.[41–43] The grain boundary contribution for a typical 1-μm grain size is about four orders of magnitude greater than the lattice contribution. Data derived from an Al_2O_3 scale growth model for FeCrAl–Y_2O_3 oxidation also predicts grain boundary dominance over lattice diffusion.[44]

Aluminum transport in the lattice is considerably faster than oxygen.[45] No direct measurements of aluminum boundary diffusion are available. For typical Al_2O_3 scale grain sizes of 1μm, aluminum lattice diffusion can be on the same order as the oxygen boundary contribution, with increasing importance as the grain size increases (and vice versa). This is especially true when compared against the oxygen boundary coefficients calculated from actual Al_2O_3 scale growth models.[44] Changes in grain size with time, temperature, or position in the scale can be significant (Fig. 11) and need to be addressed in any diffusional growth model.[41]

The question of whether Al_2O_3 scales grow inward by oxygen diffusion or outward by aluminum diffusion can only be answered unequivocally by tracer oxidation experiments.[46] The few studies available indicate that oxygen boundary diffusion does indeed predominate at high temperatures (1100 °C, 2010 °F) for

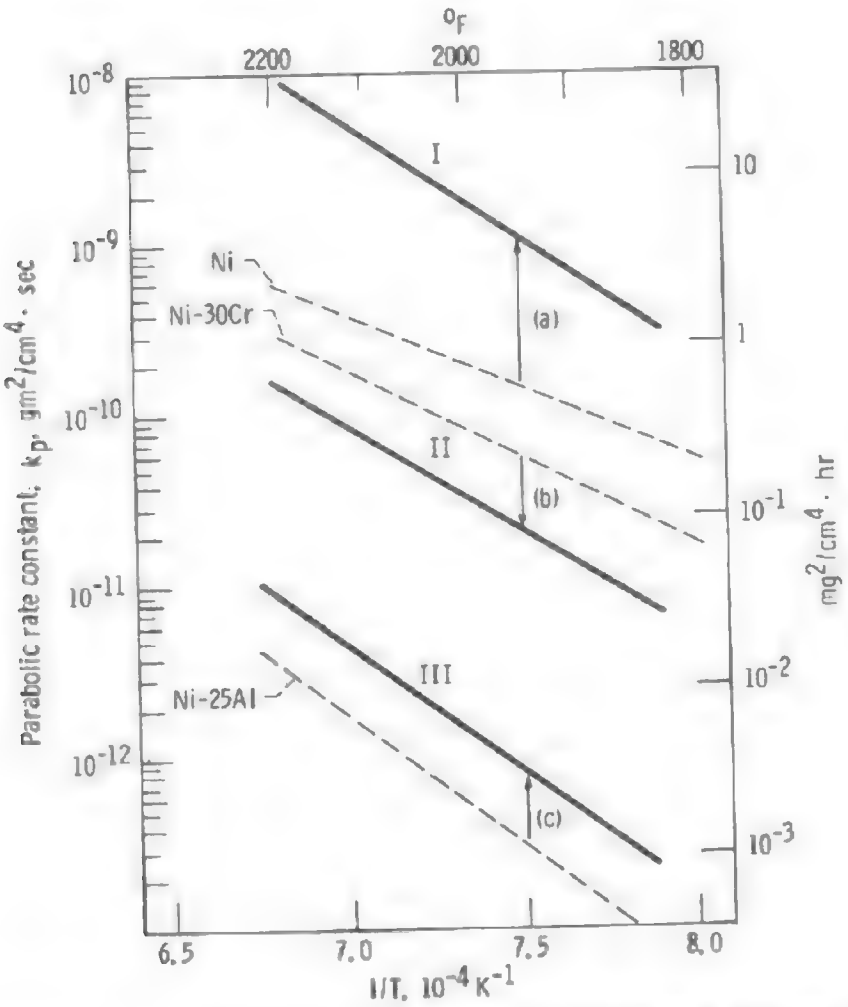

Fig. 10. Comparison of the oxidation kinetics of NiCrAl alloys (groups I, II, and III) with pure Ni, Ni–Cr, and Ni–Al alloys; Arrhenius plots.[30]

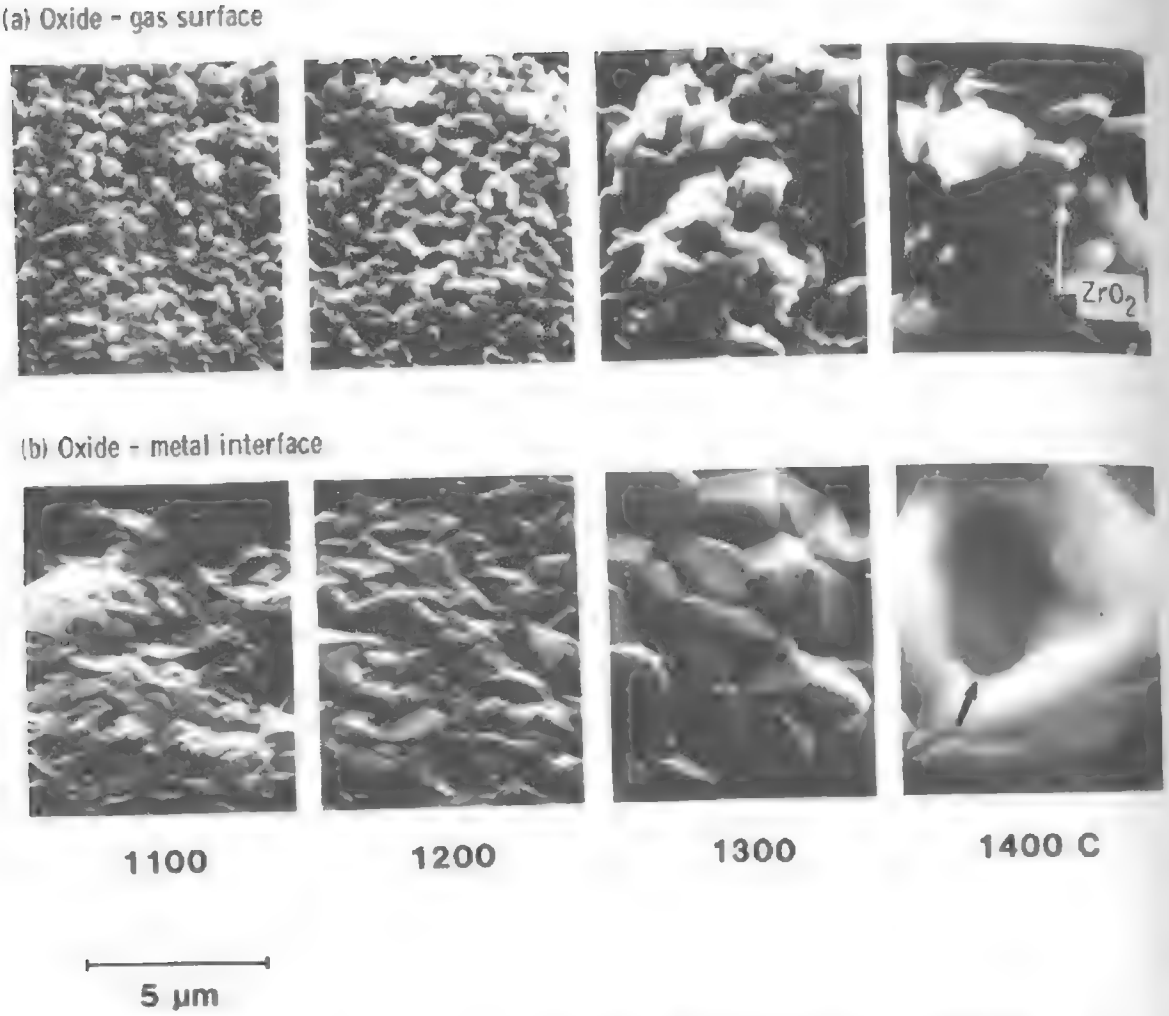

Fig. 11. Development of Al_2O_3 grains upon oxidation of FeCrAl+Zr at high temperatures for 100 h. (a) Oxide-gas surface and appearance of ZrO_2 precipitates. (b) Oxide–metal surface and dimples in centers of large Al_2O_3 grains.

NiCrAl + Y (or Zr).[47] However, some aluminum outward growth is observed, which gains in significance for low dopant values or low temperatures (900 °C, 1650 °F) where metastable transition aluminas and fast-cation transport are common.[38,48-50] Aluminum diffusion appears to be significant for undoped β-NiAl in 1100 °C, 3 h oxidation.[46]

Al_2O_3 scales show very low bulk solubilities for the much larger cations used as dopants. This results in segregation to oxide grain boundaries and precipitation of yttrium, zirconium, and thorium grain boundary oxides here (Fig. 11).[44,51] The precise effect of segregation on oxygen or aluminum boundary diffusion has not been measured but is likely to be considerable.

Dopant Effects on Kinetics, Morphology, and Adhesion. For alloys with no dopants, oxidation results in nonadherent Al_2O_3 films which spall cleanly at the oxide–metal interface. The addition of about 0.01–0.1 wt. % oxygen-active or-rare earth elements (including but not limited to Sc, Y, Zr, La, Hf, Ce, Yb, and

Th) results in strongly adherent scales. The effects of dopant level on isothermal and cyclic oxidation are summarized schematically in Fig. 12 for CoCrAl+Y, Hf and NiCrAl+Zr.

Region I. Small additions are found to reduce somewhat the rate of scale growth (Fig. 12) and the amount of compressive growth stress within the scale.[52–55] The reduction in scale weight is attributed to a decrease in the amount of compressive buckling and total amount of oxide area as opposed to oxide thickness, as shown in Figs. 13a,b. This observation is often related to a growth stress argument based on production of oxide within the scale at its grain boundaries.[56–58] It is supported by tracer studies that found ^{18}O buildups within preexisting scales on undoped alloys of NiAl.[46] This suggests that new oxide can be formed within the scale and that aluminum outward diffusion is responsible for growth stress and buckling. At very low dopant levels interfacial porosity can be effectively eliminated (Fig. 13b).[52,56,59] Finally, oxide adherence is conferred rather precipitously with dopant level as indicated by the amount of total oxidation in cyclic tests (Fig. 12).

Region II. These alloys exhibit the optimum combination of isothermal and cyclic performance having both excellent adherence and minimal growth rates. Buckled scales and convoluted metal surfaces give way to flat interfaces and no voidage (Figs. 13b,c). Fingerlike Al_2O_3 protrusions (pegs) initiated by dopant-rich oxides grow from the oxide–metal interface into the alloy.[52–54]

Region III. High dopant levels cause excessive weight gains due to subscale formation (Figs. 12 and 13d). Exceeding the solubility limit of the dopant element X often results in nonprotective oxidation of coarse M–X precipitates to form voluminous Al–X mixed oxides.[60]

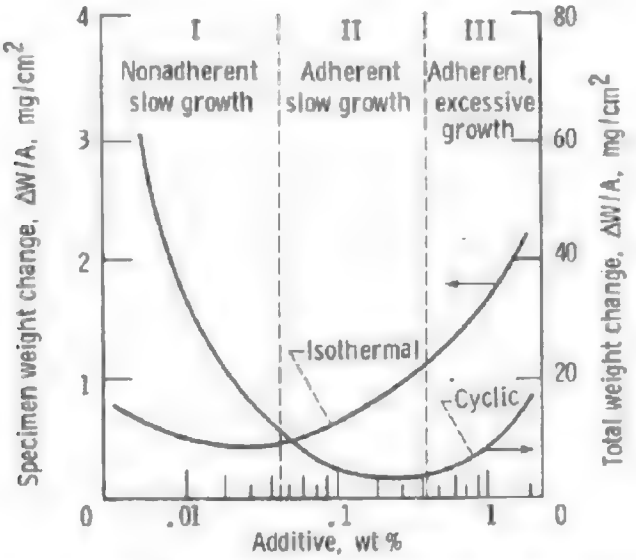

Fig. 12. Schematic comparison of oxygen-active dopant effects on isothermal and cyclic oxidation [NiCrAl+Zr and CoCrAl+Y, Hf alloys, 1200 °C (2200 °F) for 100 h].[52–54]

The boundaries of the three regions do not occur at a fixed or consistent value of the dopant level for different base alloys or oxidation temperatures. Consequently, the minimum dopant levels required to impart adhesion vary considerably,[52-57,61-63] and no universal optimum level exists. A simple generalization is that 0.1 wt. % is usually sufficient for adhesion and 1.0 wt. % usually results in excessive subscales.

Adherence Models. The models most often quoted to explain adhesion are listed as 1–4 in Table 1, as discussed elsewhere.[64] They have basically evolved from explanations of regions I, II, and III behavior and remain controversial. Much of the controversy arises from three factors. First, each possesses a certain degree of elegance because it is consistent with most of the kinetic, morphological, and adherence effects. Second, despite this agreement, there is at least one inconsistency between observed adherence and the mechanism by which adherence is proposed. For example, adherence without pegs, spalling without voids, spalling without stressed or buckled scales, and adherence in highly deformed scales have all been observed.[56,59,61] Third, partial contributions to adherence may indeed occur from all four models.

The most recent model (5 in Table 1) is based on the observation that sulfur segregation to the oxide–metal interface can be prevented by the oxygen-active

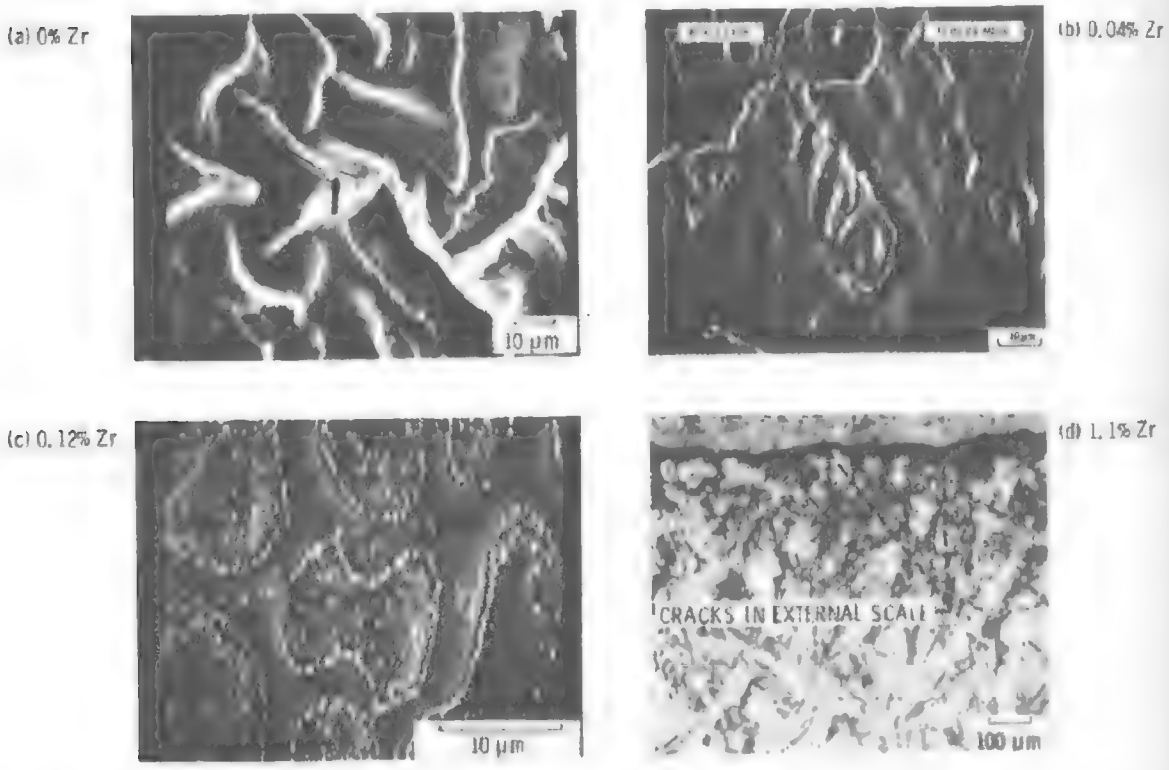

Fig. 13. Changes in scale morphology with Zr dopant level in NiCrAl alloys. (a,b,c) 8 h at 1100 °C (2010 °F); (d) 200 h at 1200 °C (2200 °F). (a) 0% Zr, buckled and cracked (arrow) scale. (b) 0.04% Zr, partial spalling and rumpling, no voids. (c) 0.12% Zr, no spalling or buckling. (d) 1.10% Zr, excessive subscale formation.[47,53]

Table 1. Models of Al_2O_3 Scale Adherence

Designation	Dopant effect
1) Pegging:	Oxide intrusions mechanically key scale
2) Vacancy sink:	Interfacial voids prevented by vacancy accommodation
3) Growth stress:	Al^{3+} counterdiffusion and growth within oxide prevented
4) Scale plasticity:	Finer Al_2O_3 grains, higher D_{gb} promote stress relief by Coble creep
5) Chemical bond:	Sulfur "bond poison" gettered by dopants

dopants.[65 68] The role of sulfur here is believed to be analogous to sulfur grain boundary embrittlement of metals caused by capturing metal atom electrons and "poisoning" the bond.[69] Additional strong support for this proposal comes from experiments where adherent scales are produced for NiCrAl alloys having *no* oxygen-active yttrium, hafnium, or zirconium dopants by simply reducing or avoiding the initial sulfur impurity.[70,71]

The observed segregation of the dopant elements themselves has spawned some speculation that this further increases the strength of the interfacial bond.[68] The chemical factors tied to successful adherence additives, as proposed in this model, are a highly negative ΔG_f (oxide) and ΔG_f (sulfide), an electron configuration with empty *d* orbitals, and a low solubility in Ni(Co,Fe).[68]

EFFECTS OF OTHER COMMON ALLOYING ELEMENTS

Superalloys contain a number of significant alloying elements in addition to chromium and aluminum, including manganese, titanium, silicon, and the refractory metals. In many instances these elements exert significant influence on the oxidation resistance of Cr_2O_3- or Al_2O_3-forming alloys. In this section the effects on model alloys will be reviewed.

Manganese, Titanium, and Silicon

Manganese may be viewed as a potential, but much less effective, replacement for chromium in establishing healing layers of Cr_2O_3 scales. Manganese promotes Cr_2O_3 formation in Ni–20Cr,[72,73] but up to 30% manganese was not effective in Co–19Cr.[74] Additions of manganese have been shown to maintain Al_2O_3 scales on Fe–Al alloys by preventing iron-rich nodular eruptions.[75,76]

Additions of titanium promote Cr_2O_3 formation on both Ni–20Cr and Co–20Cr but do not significantly affect the Cr_2O_3 growth rate.[77,78] Adherence has been reported to degrade on Ni–20Cr, improve on Ni–50Cr, and remain unchanged on Co–20Cr when titanium is added.[78-80]

Titanium slightly increases the growth rate of Al_2O_3 scales on β-NiAl and does little to promote exclusive Al_2O_3 formation on γ′-Ni_3Al or γ-Ni(Al) alloys.[40,81] Titanium has a deleterious effect on adherence on a nickel-base superalloy[82] but improves it on Fe–18Cr–6Al.[83]

Of all the elements with oxygen reactivity intermediate between that of aluminum and nickel, silicon causes the most dramatic beneficial effects. The isothermal and cyclic behavior of some Ni–Cr, Fe–Cr, and Ni–Al alloys can be improved by silicon so as to equal the performance of exclusive Cr_2O_3- or Al_2O_3-forming alloys.[40,81,84] These benefits stem from the formation of SiO_2 subscales and the prevention of Ni(Fe) oxides. Additions of 0.5–1.3% silicon are very beneficial to B-1900, improving its cyclic oxidation resistance to the level of an aluminide coating on B-1900.[85] Similar additions to MAR-M 200 and IN-713 also caused improvements but not to the same extent as B-1900.[86] However, these benefits could not be made practical in that the silicon additions severely degraded mechanical properties even at the 0.5% level. Silicon has also found increasing usage in protective coatings based on NiCr or NiCrAl systems.[87] High-silicon coatings actually rely on the formation of a protective SiO_2 scale that can be as slow growing as Al_2O_3 films for certain Ni–Cr–Si compositions.[88] Smaller silicon additions to conventional PVD Ni–Cr–Al coatings are also used, presumably to stabilize Al_2O_3 scale formation for a longer period of time.

Effects of Refractory Elements

Refractory elements such as molybdenum, tungsten, and tantalum are used rather extensively in nickel- and cobalt-base superalloys as strengtheners, participating in γ′ formation, carbide formation, and through solution effects. Other refractory elements such as columbium, hafnium, and zirconium are also utilized for strengthening purposes including the formation of Ni_3Cb.

The literature, which has recently been reviewed,[89] indicates that the refractory elements can produce three effects on the oxidation of nickel- and cobalt-base alloys. One effect is beneficial and arises since these elements can be considered to be oxygen getters and assist in the formation of Al_2O_3 and Cr_2O_3 healing layers. The other two effects are deleterious. First, refractory elements decrease the diffusion of aluminum, chromium, and silicon, which opposes healing layer formation. Second, the oxides of the refractory metals are generally nonprotective (i.e., low melting points, high vapor pressure, high diffusivities, etc.) and are consequently undesirable as components of external scales. Thus, the deleterious effects produced by the refractory metals outweigh the beneficial effects and, therefore, they are not usually added to superalloys to improve oxidation behavior. On the other hand, some of these elements do appear to be preferable to others. For example, tantalum does not appear to produce deleterious effects as severe as do tungsten or molybdenum, and hence is probably one of the preferred refractory elements. Tungsten, molybdenum, and vanadium are similar, but tungsten does evidently decrease alloy interdiffusion rates more than the other elements and therefore may have more of an adverse effect on selective oxidation. Columbium oxides are not protective and the presence

of this element in oxide scales is not desired. Rhenium has been used in superalloys to a limited extent and appears to exert similar effects. Hafnium and zirconium are often present in superalloys at low concentrations and significantly improve the adherence of oxide scales.

COMPLEX NICKEL-BASE SUPERALLOYS

The many alloying elements in superalloys over and above the NiCrAl-base compositional variations, provide such a diversity in oxidation behavior that classification into a few simple categories is at present impossible. Therefore, the specific behavior of individual alloys and an attempt at some broad generalization is presented.

General Mechanisms

Kinetics. The description of the oxidation kinetics of superalloys by gravimetric data is complicated in that substantial fractions of the total scale are produced during a linear rate transient period ($\leq$2 h). This is often followed by more than one parabolic regime requiring two or three rate constants, which precludes a simple comparison of alloys.[90–92] The temperature dependence of the first parabolic constant, k_{pI} (Fig. 14) indicates the rates for most superalloys fall between that for Cr_2O_3 growth (Ni–30Cr),[8] and Al_2O_3 growth (Ni–14Cr–12Al).[30] Most of the superalloy rates are within a factor of 2 of each other at 1800 °F, and the activation energies are closer to that for Cr_2O_3 growth ($\simeq$60kcal/mol) than for Al_2O_3 ($\simeq$120 kcal/mol).[90–99] No consistent behavioral trend is apparent as the composition varies from high Cr, low Al to low Cr, high Al as would be predicted from oxidation maps for ternary Ni–Cr–Al alloys, nor do any of these alloys approach the oxidation resistance of exclusive α-Al_2O_3 formers, thus indicating the influence of elements other than chromium and aluminum.

Scale Components. The changes in rate parameters are linked to changes in the oxide phases comprising the scale, as shown in the time–temperature–oxide map for Udimet 700 (Fig. 15). The initial linear region (1) is characterized by a thin film of Al_2O_3 which is being overgrown by colonies of Cr_2O_3 originating at alloy grain boundaries.[90] Upon completion of this process, parabolic kinetics ensue and internal oxidation is observed, region 2. During the entire process depletion zones are formed ahead of the oxidation front by selective removal of the active elements (usually Al, Ti, and Si). Depletion zones and internal oxidation fronts also adhere to parabolic growth rates, which increase with temperature.

A secondary parabolic rate, k_{pII}, may occur for some alloys[92] and is usually lower than k_{pI}. Extended oxidation of Udimet 700 is characterized by $NiCr_2O_4$, NiO, and TiO_2 overgrowths at the gas–$(Cr,Al)_2O_3$ surface, region 3. A peculiar feature of Udimet 700 is the formation of a protective $Ni(Al,Cr)_2O_4$ spinel scale at ~1900 °F (1030 °C). This scale prevented overgrowths and resulted in a growth rate *less* than that at 1800 °F (982 °C).

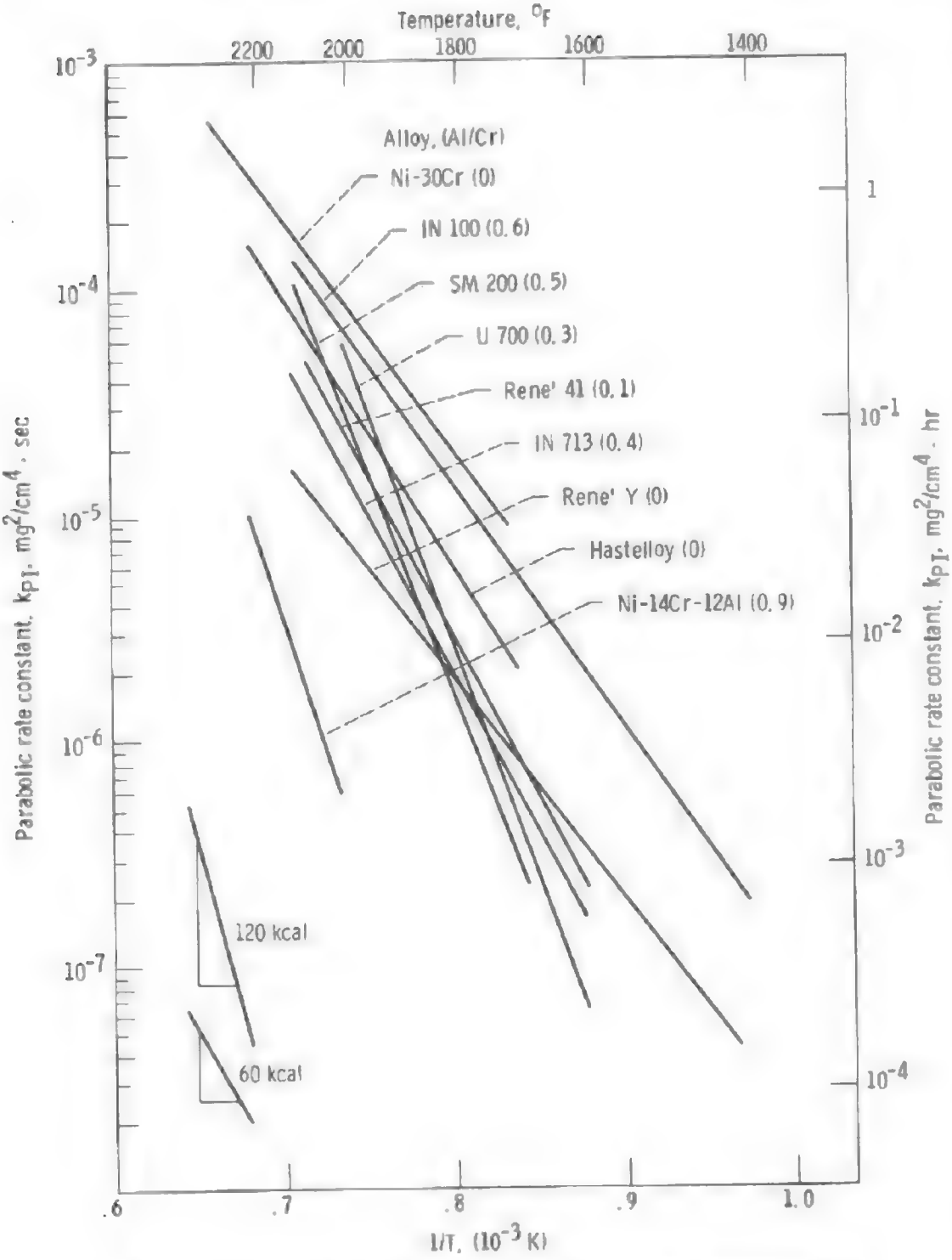

Fig. 14. Temperature dependence of $k_{p,l}$ for commercial superalloys.[90–96]

The three oxidation regimes for a number of alloys are summarized in Table 2. Oxides Al_2O_3, Cr_2O_3, or SiO_2 are often the thin initial scales in region 1. These oxides, coupled with TiO_2 or TiN, also make up most of the internal oxide phases that appear throughout stages 2 and 3. Advanced oxidation (3) is often characterized by the appearance of (Ni or Mn) (Al or $Cr)_2O_4$ spinels, NiO, and TiO_2 and $NiTiO_3$. This chart emphasizes the complexity of the scales and scale evolution schemes for common superalloys. The widespread occurrence of nickel-containing oxides pos-

sessing high diffusivities accounts for the high oxidation rates with respect to NiCrAl in Fig. 14.

Performance–Mechanism Correlations

The complex nature of superalloy oxidation and the relative performance of four superalloys as a function of time, temperature, aluminum and chromium content, refractory metal content, and type of test (static vs. high velocity, isothermal vs. cyclic) have been identified in a series of comparative studies.[97–101] The isothermal and cyclic oxidation performance of B-1900 and NASA-TRW VIA at 900–1100 °C (1650–2010 °F) was generally excellent; IN-713C was intermediate, and IN-738X was poor by comparison. For example, the total surface degradation, defined as alloy consumption plus depletion zone, was only ~1 mil for B-1900 and VIA after 100 h cyclic oxidation at 1100 °C. This is in comparison to 3.5 mils for IN-713C and 12.7 mils for IN-738X. Parallel trends in the isothermal and cyclic weight change were also observed.

The overall correlations of alloy composition, oxide phase content, and performance can be seen in Fig. 16. Here the type (a) oxides (Al_2O_3, $NiAl_2O_4$, and MR_2O_6) are associated with better performance compared to type (b) oxides (Cr_2O_3, $NiCr_2O_4$, and $NiTiO_3$). These phases are ultimately tied to the alloy compositions designated as types (a) or (b), that is, (Al+R) or (Cr+Ti), where R = Cb, Ta, W, Mo.

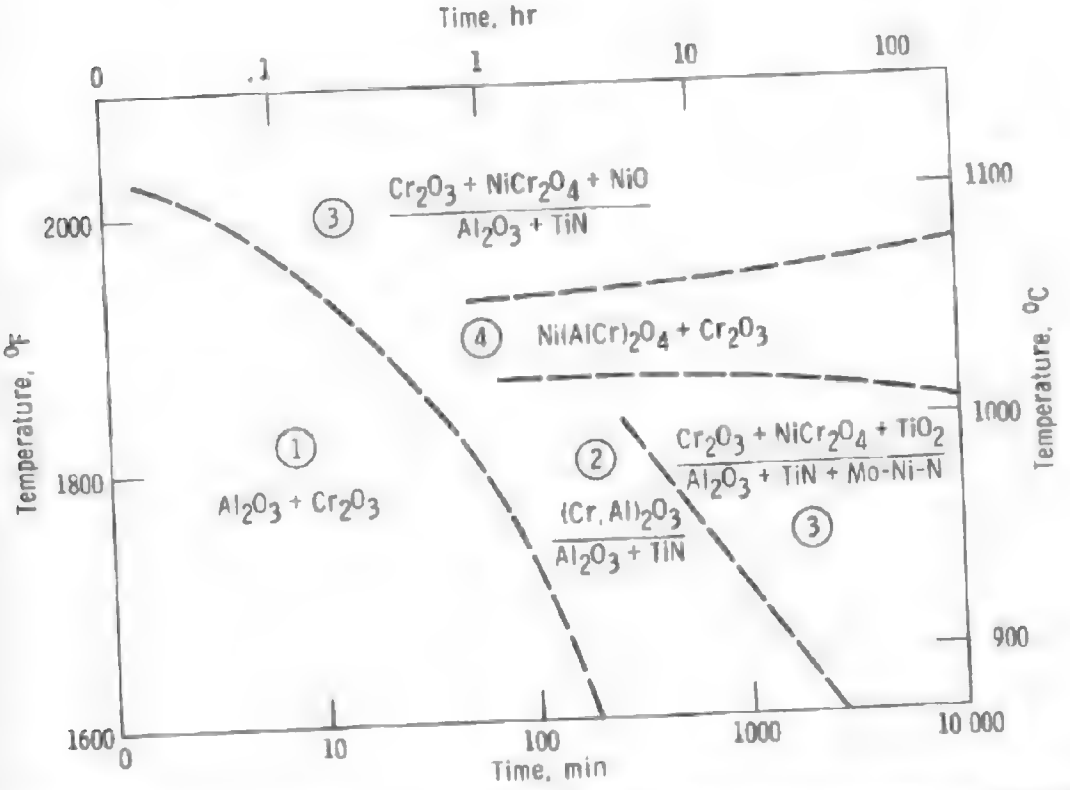

Fig. 15. Map of scale constituents for isothermal oxidation of Udimet 700: (external scale)/[(internal oxides) + subscale].[90]

Table 2. Oxidation Stages of Superalloys[a]

Low temp, short time ⟶ High temp, long time

	(1)	(2)	(3)
RENE' Y (22Cr,1Si,1Mn,9Mo)	Cr_2O_3	$\frac{Cr_2O_3 + MnCr_2O_4}{SiO_2 + Mn_xO_y}$	$\frac{MnCr_2O_4 + Cr_2O_3 + NiO}{SiO_2 + Mn_xO_y}$
HASTELLOY X (22Cr,1Si,0.5Mn,9Mo)	$Cr_2O_3 + NiCr_2O_4 + SiO_2$		$\frac{Cr_2O_3 + NiCr_2O_4}{SiO_2 + NiCr_2O_4}$
RENE' 41 (20Cr,1Al,3Ti,10Mo)	$Al_2O_3 + Cr_2O_3$	$\frac{(Cr,Al)_2O_3}{Al_2O_3}$	$\frac{Cr_2O_3 + NiCr_2O_4 + NiO + (TiO_2)}{Al_2O_3 + TiN}$
UDIMET 700 (15Cr,4Al,4Ti,4Mo)	$Al_2O_3 + Cr_2O_3$	$\frac{(Cr,Al)_2O_3}{Al_2O_3 + TiN}$	$\frac{Cr_2O_3 + NiCr_2O_4 + NiO + (TiO_2)}{Al_2O_3 + TiN}$
IN 713 C (14Cr,6Al,1Ti,6Mo)	$NiCr_2O_4 + NiO + Cr_2O_3$	$\frac{NiCr_2O_4 + (Cr_2O_3)}{Al_2O_3}$	$\frac{Al_2O_3 + NiAl_2O_4 + (NiCr_2O_4)}{TiO_2 + Cr_2O_3 + (TiN)}$
SM 200 (9Cr,4Al,2Ti,12W)	Cr_2O_3	$\frac{Ni(Cr,Al)_2O_4 + TiO_2 + NiO}{Al_2O_3}$	$\frac{NiCr_2O_4 + NiAl_2O_4 + NiWO_4 + NiTiO_3}{Al_2O_3 + TiO_2 + TiN}$
IN 100 (10Cr,6Al,4Ti,3Mo)	$NiO + TiO_2$	$\frac{(Ni,Co)O + (Ni,Co)Cr_2O_4 + NiTiO_3}{Al_2O_3 + TiO_2 + (TiN)}$	$\frac{NiCr_2O_4 + NiTiO_3 + NiAl_2O_4 + Al_2O_3}{TiO_2 + TiN}$

EXTERNAL SCALE
INTERNAL OXIDES OR SUBSCALE
( ) = present in part of region (3)

[a]1400–2200 °F (760–1200 °C), 1–10^5 min. isothermal (from refs. 90–92).

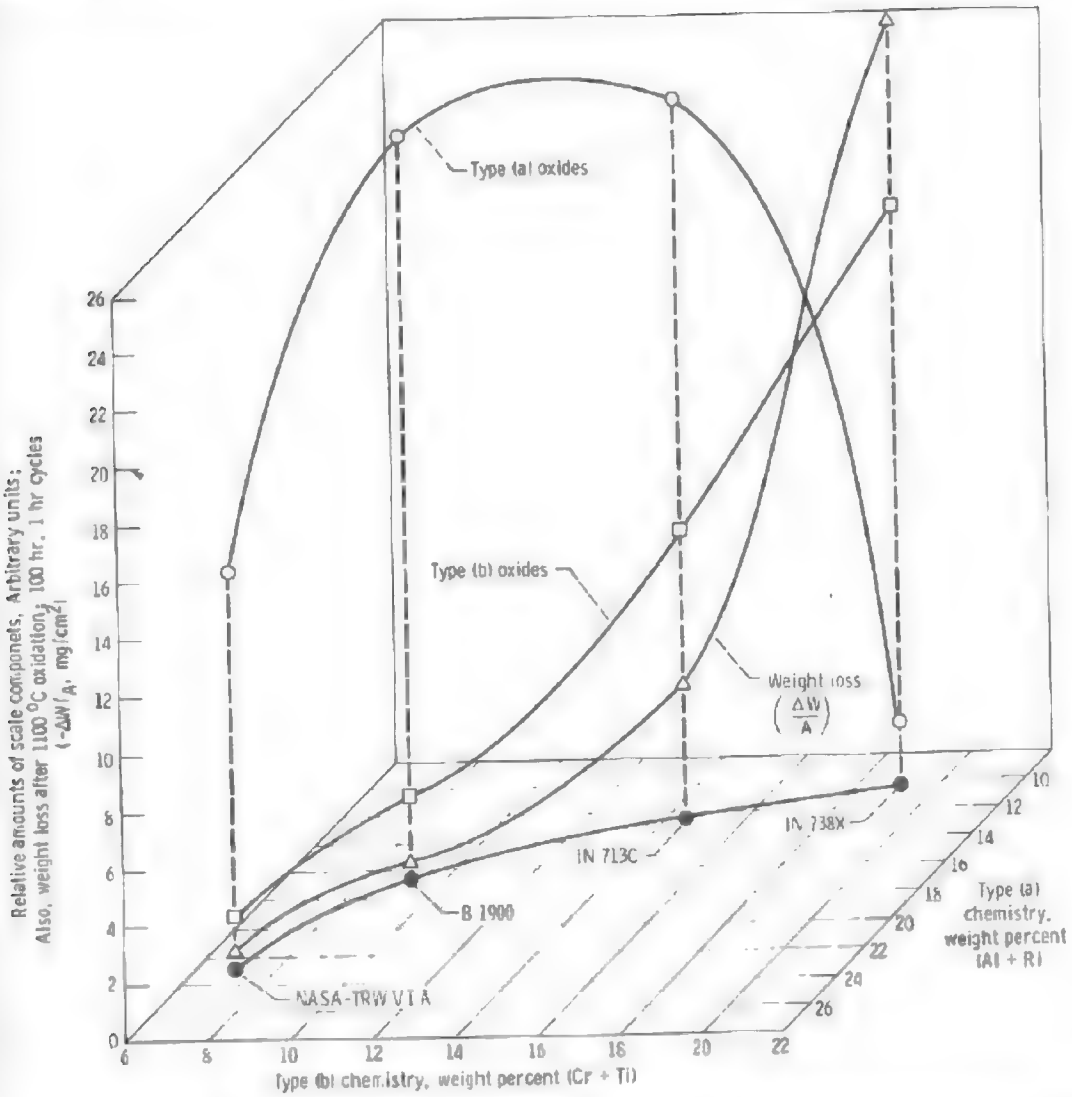

Fig. 16. Dependence of oxidation behavior and scale constituents on the composition of four superalloys.[97,98]

The tri-rutile or tapiolite MR_2O_6 oxides may be beneficial in assisting Al_2O_3 healing layers and preventing NiO overgrowths. The role of $NiTiO_3$ and TiO_2 is not known. However, substantial titanium enrichment is usually associated with the outer surface of the scales, especially for IN-713C and IN-738X, as shown in Fig. 17. Evident are a titanium-containing outer layer of Cr_2O_3 and $NiCr_2O_4$, internal oxide fingers of $NiTa_2O_6$ and Al_2O_3, and the γ alloy depletion zone denuded of γ' particles. Variations on this microstructure exist for the other alloys; in the extreme B-1900 exhibits only a thin $Al_2O_3+NiAl_2O_4$ external scale.

The changes in oxidation behavior with time, temperature, and cycling are difficult to generalize for all alloys and conditions. Low-temperature (900–1000 °C, 1650–1830 °F) or isothermal conditions often favor the formation of Al_2O_3 scales, while higher temperature (1100 °C, 2010 °F) or cycling promotes NiO, $NiCr_2O_4$, and Cr_2O_3 in comparison. The major scale constituents increase monotonically with time, except for IN-738X, where Cr_2O_3 reaches a maximum and then is overtaken by substantial NiO and $NiCr_2O_4$ scales that ultimately cause breakaway cyclic behavior.[97] In these four cases high aluminum and refractory

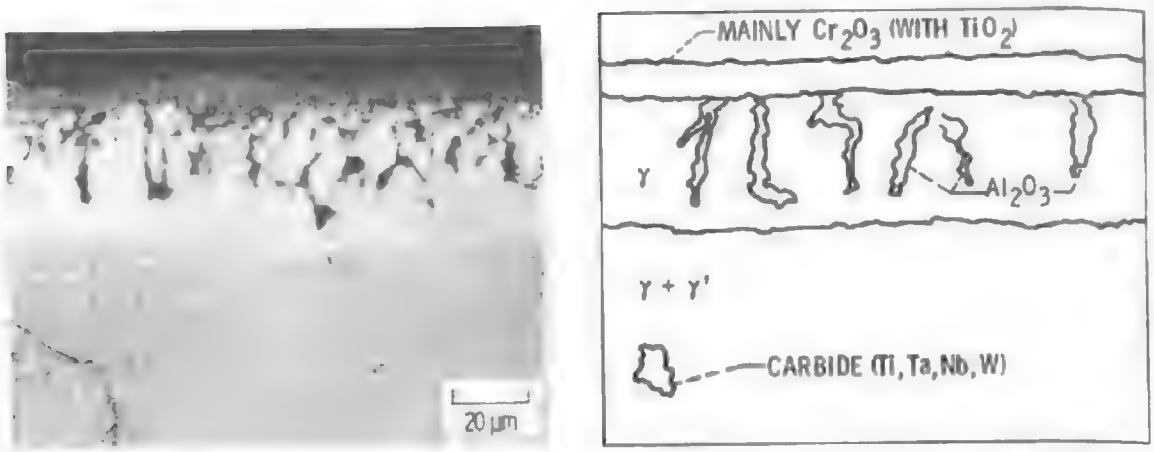

Fig. 17. Microstructure of IN-738 after 24 h oxidation at 975 °C (1790 °F) showing outer Ti-rich Cr_2O_3 scale, internal oxidation, and depletion zones.[100]

metal content appear preferable to high chromium or titanium. This basic theme repeats itself in the following discussion of compositional effects. However, it is emphasized that these rules must be applied with caution to avoid overgeneralization. It is not only the elements taken individually but the combined effects of many complex interactions *between* the elements that fully determines oxidative behavior of commercial superalloys.

Effects of Multielement Variations

Model Alloys (Statistical Studies). The precise compositional effects on the oxidation mechanisms of complex superalloys involve multielement interactions that are beyond present-day understanding. However, cyclic oxidation performance (weight change) was successfully correlated with systematic multielement variations in two extensive, statistically designed studies.[102,103] In the first study seven elements were varied at two levels; in the second study five elements were varied at five levels, amounting to nearly 100 alloys in all. The metal consumption of each alloy was described by an attack parameter, K_A, which takes into account both the growth and spallation of scales. Multiple linear regression analysis produced equations relating K_A to composition for each study.

Insights are also gained by ranking the alloys numerically from best to worst and identifying compositional trends.[104] A summary of one such ranking is shown in Table 3. In (a) the alloys are grouped by performance, the average values of performance and composition shown, and consistent trends within a group (if any) identified in boldface. This technique illustrates that all the best groups are consistently high in aluminum. Also the performance decreases by orders of magnitude if the aluminum content is decreased. Part (b) presents some specific alloys that were selected to represent the extremes of either performance or composition.

Taken together, these charts from both studies allowed the following conclusions:

1. High aluminum (6%) is the most important factor for good performance.
2. High chromium (15%) is not always needed for good performance.

Table 3. Cyclic Oxidation Ranking and Compositional Trends for Model Superalloys[a]

(a) Group averages[a]

Rank (group), number	$\overline{\Delta W/A}_{100\ hr}$, mg/cm^2	$\overline{K_A}$	Al 3.2/6.2	Cr 6.0/18.0	Ti 1.0	Co 0/20	Cb 1.0	Ta 0/8.0	Mo 0/4.0	W 2.0	Generalization
(a) 1-7	-1.7	.46	**5.5**	**11.6**	1.0	9.3	1.0	**5.4**	**1.6**	2.0	High Al, high Ta
(b) 8-13	-3.1	.76	**5.5**	**13.0**	↓	8.3	↓	**4.7**	**3.0**	↓	High Al, high Ta, high Mo
(c) 14-19	-7.6	1.8	**5.3**	**13.0**		8.3		3.3	2.3		High Al
(d) 20	-12.	2.8	4.8	12.0		**10.0**		**4.0**	**2.0**		Midpoint composition, 8 replicates
(e) 21-29	-28.	7.5	4.8	13.0		10.6		3.8	1.7		
(f) 30-38	-150.	42.	**4.0**	**13.7**		10.6		3.3	2.1		Low Al, high Cr
(g) 39-45	-476.	108.	**4.0**	**9.0**	↓	**9.3**	↓	3.7	2.1	↓	Low Al, low Cr

(b) Specific endpoint compositions[b]

(a) 1	-1.4	.30	5.5	15.0	1.0	15.0	1.0	6.0	1.0	2.0	High Al, low Mo, high others
(b) 2	-1.7	.32	5.5	9.0	↓	15.0	↓	6.0	3.0	↓	High Al, low Cr, high others
(c) 9	-2.9	.73	5.5	15.0		15.0		6.0	3.0		High Al, high others
(d) 20	-12.	2.8	4.8	12.0		10.0		4.0	2.0		Midpoint composition
(e) 33	-90.	29.	4.0	15.0		5.0		2.0	1.0		Low Al, high Cr
(f) 43	-496.	114.	4.0	9.0		5.0		2.0	1.0		Low Al
(g) 45	-748.	158.	4.0	9.0	↓	5.0	↓	2.0	3.0	↓	Low Al, high Mo

[a]Boldface represents consistent trend within group.
[b]Boldface represents high levels.

[a]1100 °C (2010 °F), 100 h, 1-h cycles. (a) Group averages. (b) Specific endpoint compositions. (From refs. 103 and 104.)

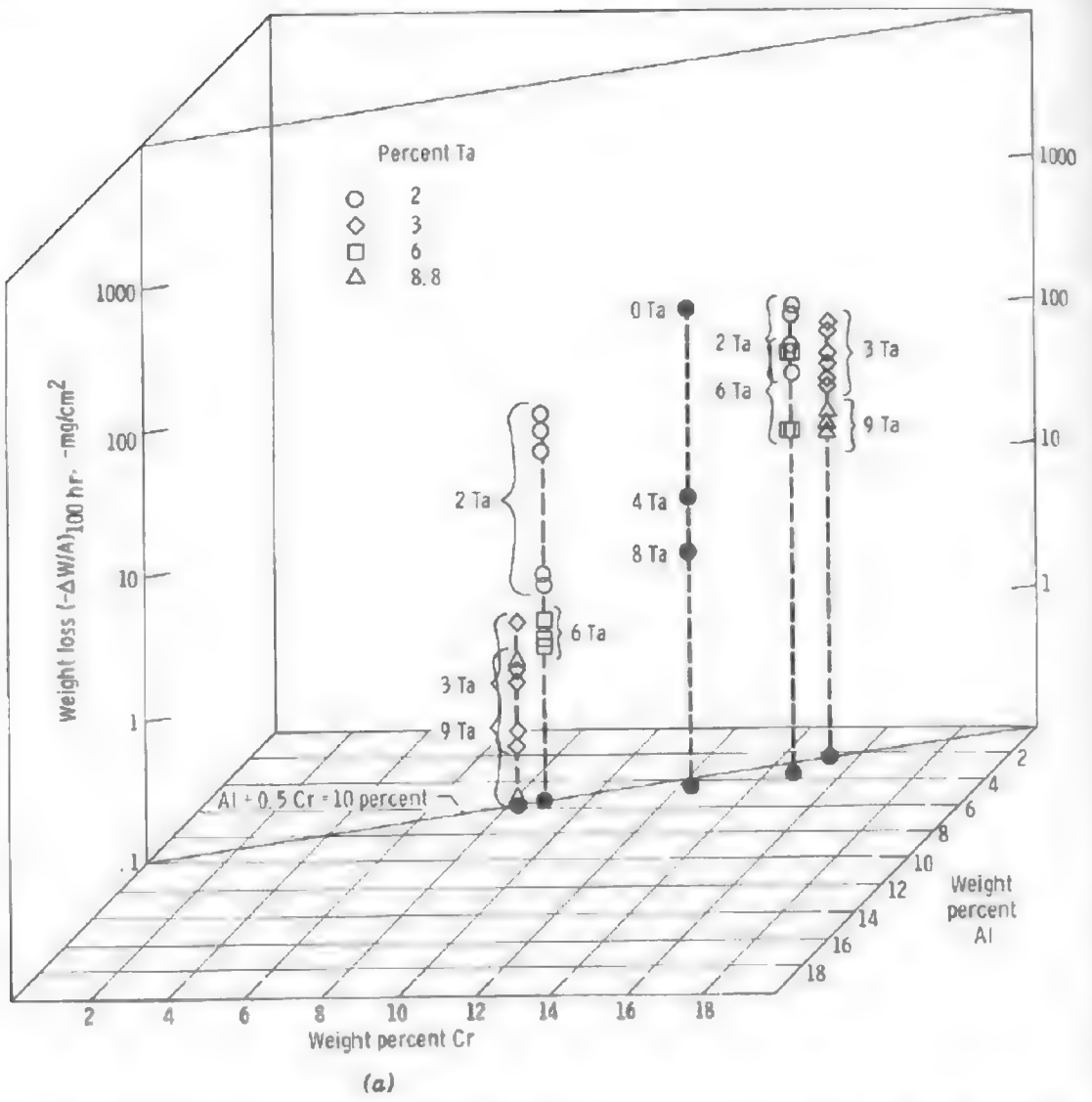

Fig. 18. Multielement oxidation maps illustrating some compositional trends that affect the cyclic oxidation of superalloys [1100 °C (2010 °F), 100 h, 1-h cycles]. (a) Beneficial trends with high Al and Ta for model superalloys.[102–104]

3. High chromium (15%) cannot compensate for low aluminum (2–4%).
4. Tantalum (3–9%) appears in best groupings and alloys.
5. Low titanium (<2%) appears in most of the better alloys.

The apparent beneficial effect of tantalum is shown graphically in the multielement oxidation map in Fig. 18a, where the higher tantalum alloys consistently exhibited less weight loss compared to other alloys of the same Al–Cr levels. However, as is the case for chromium, tantalum cannot fully compensate for lower aluminum contents (<5%). To allow direct comparison, the alloys shown here have Cr–Al contents in the range of cast superalloys where $Al + \frac{1}{2}Cr = 10 \pm 2$. Further generalization regarding, cobalt, columbium, molybdenum, and tungsten becomes dangerous because of the complex multielement interactions. These charts also identified

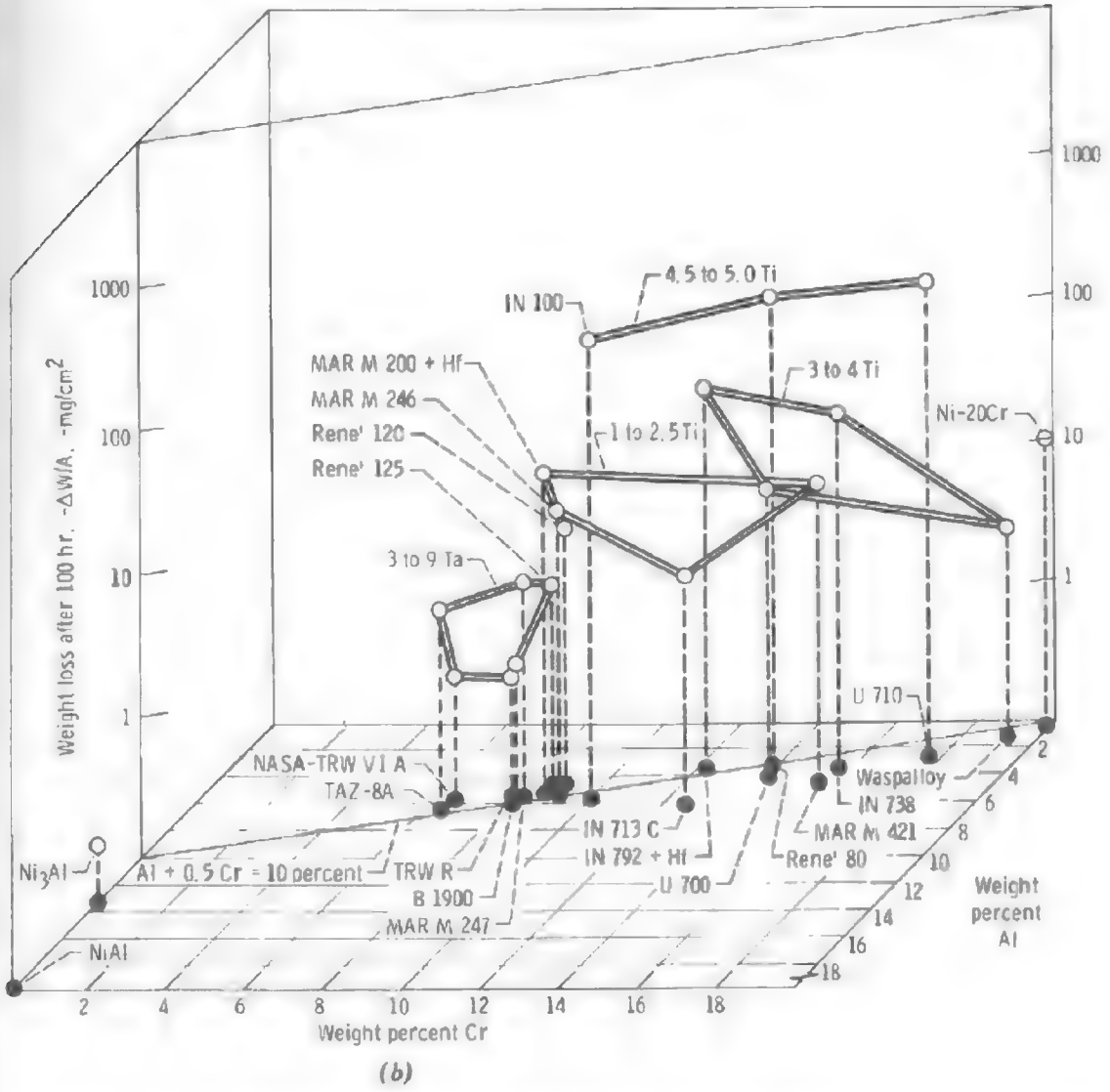

Fig. 18. *(Continued)* (b) Beneficial trends with high Al and Ta and low Ti for commercial superalloys.[104,105]

optimum alloys with weight losses <2 mg/cm^2 after 100 h, representing extremely good oxidation resistance, that is, surface recession < 0.1 mils per side.

The oxide phases produced by these alloys were broadly grouped into Al_2O_3, $NiAl_2O_4$, and $Ni(Ta,Cb,W,Mo)_2O_6$ tri-rutiles for the high-aluminum alloys and NiO, $NiCr_2O_4$, and $Ni(W,Mo)O_4$ for the low-aluminum alloys. This again illustrates the desirability of aluminum-containing oxides as well as the acceptability of the tri-rutile refractory metal oxide.

Commerical Superalloys. A similar ranking analysis for ~20 commercial superalloys is presented in Table 4. The alloys are arbitrarily grouped into classes whose average weight loss after 100 h, 1100 °C (2010 °F) cyclic oxidation increases about threefold from group to group. Compositional effects are much more difficult

Table 4. Cyclic Oxidation Groupings and Compositional Trends for Commercial Superalloys.[a]

Group	Alloy	$(-\Delta W/A)_{100hr}$ $-mg/cm^2$	Al	Cr	Cb	Ta	Mo	W	Ti	Co	Zr	Hf
A	NASA TRW VI A	.6	5.4	6.1	0.5	9.0	2.0	5.8	1.0	7.5	0.13	0.4
	TRW R	.6	5.3	8.1	.3	6.3	2.8	4.0	.8	8.0	0.12	1.1
	B 1900	.9	6.0	8.0	---	4.0	6.0	----	1.0	10.0	0.1	----
	B 1900 + Hf	1.3	6.0	8.0	---	4.0	6.0	----	1.0	10.0	0.1	1.5
B	TAZ 8A	2.7	6.0	6.0	2.5	8.0	4.0	4.0	---	----	1.0	----
	RENE' 125	2.7	4.9	8.7	---	3.8	1.7	7.1	2.4	10.1	.05	1.5
	WASPALLOY	2.9	1.3	19.5	---	---	4.3	----	3.0	13.5	.06	----
	MAR M 247	3.0	5.5	8.2	---	3.0	.6	10.0	1.0	10.0	.09	----
	IN 713 C	5.5	6.1	12.5	2.0	---	4.2	----	.8	----	.10	----
	RENE' 120	6.4	4.3	9.0	---	3.8	2.0	7.0	4.0	10.0	----	0.1
C	UDIMET 700	10.0	4.0	14.2	---	---	4.9	----	3.9	16.4	.02	----
	MAR M 246	10.0	5.5	9.0	---	1.5	2.5	10.0	1.5	10.0	.05	----
	MAR M 421	12.4	4.3	15.8	2.0	---	2.0	3.8	1.8	9.5	.05	----
	MAR M 200 + Hf	16.4	5.0	8.6	.9	---	---	11.7	1.8	9.2	.03	2.0
	MAR M 200	17.4	5.0	9.0	1.0	---	---	12.0	2.0	10.0	.05	----
D	IN 738	31.2	3.4	16.0	0.9	1.7	1.7	2.6	3.4	8.5	.10	.10
	IN 792 + Hf	45.2	3.3	12.3	.0	3.9	1.9	4.1	4.0	8.9	.07	.07
	IN 939	79.4	1.9	22.4	1.0	1.4	---	2.1	3.7	19.0	.11	----
E	IN 100	164.	5.5	10.0	---	---	3.0	----	4.7	15.0	.06	.06
	RENE' 80	187.	3.0	14.0	---	---	4.0	4.0	5.0	9.5	.03	.03
	UDIMET 710	202.	2.5	18.0	---	---	3.0	1.5	5.0	15.0	----	----
	MAR M 211	450.	5.0	9.0	2.7	---	2.5	5.5	2.0	10.0	----	.05

General trends

Al	Ta	Ti
High 5-6	High 4-9	Low 0-3
Medium 4-5	Low 0-2	Medium 2-4
Low 2-4		High 3-5

[a]1100 °C (2010 °F), 100 h, 1-h cycles (from refs. 104 and 105).

to prove because there is no systematic variation as in the statistically designed studies. Nevertheless broad trends appear (indicated as composition blocks) which parallel those already put forth: 5–6 Al, 3–9 Ta, and 0–2 Ti are characteristically present in alloys with optimum oxidation resistance.

These trends are presented graphically in the multielement oxidation map (Fig. 18b) where significant differentials in cyclic weight change are associated with aluminum, tantalum, and titanium contents. Data for binary Ni–Al and Ni–Cr alloys are shown for comparison purposes.[105] It is also useful to note that the superalloy line, Al+½Cr = 10, lies for the most part in an optimum regime of the NiCrAl map shown in Fig. 8c. This suggests the overriding effects of the many alloying elements apart from just chromium and aluminum. Furthermore, commercial alloys with high aluminum also have low chromium, and vice versa. Therefore the Cr/Al ratio, often used to describe superalloy oxidation, actually overspecifies composition. Indeed, high Al model alloys are the most oxidation resistant, irrespective of the chromium content or the Cr/Al ratio.[102–104]

The effect of substantial amounts of cobalt (20%) in many nickel-base superalloys provides another important consideration. Reducing the cobalt level to 0–5% benefited the cyclic oxidation performance of a number of alloys at or above 1100 °C (2010 °F).[106] This is consistent with the generally inferior oxidation resistance of cobalt-base alloys compared to nickel-base alloys. These phenomena arise from the fast growth rates of highly defective cobalt oxides as well as the high refractory metal and low aluminum contents typical of these alloys.

Futher optimization of the oxidation resistance of superalloys could be achieved by in-depth studies of the key elements alluded to throughout this section. However, the most demanding applications employ current alloys coated with oxidation-resistant MCrAlY or NiAl materials. These Al_2O_3-forming alloys have therefore received a greater degree of attention, which ultimately led to a more fundamental understanding of scale growth, adhesion, and degradation mechanisms than currently exists for the superalloys.

REFERENCES

1. N. Birks and G. H. Meier, *Introduction to High Temperature Oxidation of Metals*, Arnold, Baltimore, 1983.
2. C. Wagner, *Z. Phys. Chem.*, **B21**, 25 (1933).
3. R. A. Rapp, *Met. Trans.*, **15A**, 765 (1984).
4. C. Wagner, *Ber. Bunsenges Phys. Chem.*, **63**, 772 (1959).
5. D. P. Whittle, in *High Temperature Corrosion*, R. A. Rapp (ed.), NACE, Houston, TX, 1983, p. 171.
6. C. Wagner, *Z. Elektrochem.*, **63**, 772 (1959).
7. C. E. Lowell, J. L. Smialek, and C. A. Barrett, in *High Temperature Corrosion*, R. A. Rapp (ed.), NACE, Houston, TX, 1983 p. 219.
8. C. S. Giggins and F. S. Pettit, *Trans. TMS-AIME*, **245**, 2495 (1969).
9. D. P. Whittle and H. Hindam, in *Corrosion-Erosion-Wear of Materials in Emerging Fossil Energy Systems*, A. V. Levy (ed.), NACE, Houston, TX, 1983, p. 54.
10. P. Kofstad and K. P. Lillerud, *J. Electrochem. Soc.*, **127**, 2410 (1980).
11. E. W. A. Young, P. C. M. Stiphout, and J. H. W deWit, *J. Electrochem. Soc.*, **132**, 887 (1985).

12. K. Hoshino and N. L. Peterson, *J. Am. Ceram. Soc.*, **66,** C202 (1983).
13. C. Greskovich, *J. Am. Ceram. Soc.*, **67,** C111 (1984).
14. H. V. Atkinson, *Oxid. Met.*, **24,** 177 (1985).
15. D. Caplan and G. I. Sproule, *Oxid. Met.*, **9,** 459 (1975).
16. G. M. Ecer and G. H. Meier, *Oxid. Met.*, **13,** 119 (1979).
17. S. D. Sehgal and D. Swarup, *Trans. Ind. Inst. Met.*, **15,** 177 (1962).
18. T. Nakayama and Y. Watanabe, *Trans. Iron Steel Inst. Jpn*, **8,** 259 (1968).
19. E. J. Felten, *J. Electrochem. Soc.*, **108,** 490 (1961).
20. G. M. Ecer and G. H. Meier, *Oxid. Met.*, **13,** 159 (1979).
21. C. S. Giggins and F. S. Pettit, *Metall. Trans.*, **2,** 1071 (1971).
22. H. H. Davis, H. C. Graham, and I. A. Kvernes, *Oxid. Met.*, **3,** 431 (1971).
23. G. R. Wallwork and A. Z. Hed, *Oxid. Met.*, **3,** 229 (1971).
24. J. Stringer, B. A. Wilcox, and R. I. Jaffee, *Oxid. Met.*, **5,** 11 (1972).
25. O. T. Goncel, D. P. Whittle, and J. Stringer, *Oxid. Met.*, **15,** 287 (1981).
26. F. H. Stott, J. S. Punni, G. C. Wood, and G. Dearnaley, in *Proceedings of the Conference on Modifications of Surface Properties of Metals by Ion Implantation, Manchester, U.K.*, 1981, p. 245.
27. M. J. Bennett, in *High Temperature Corrosion*, R. A. Rapp (ed.), NACE, Houston, TX, 1983, p. 145.
28. C. S. Tedmon, *J. Electrochem. Soc.*, **113,** 766 (1966).
29. F. S. Pettit, *Trans TMS-AIME*, **239,** 1296 (1967).
30. C. S. Giggins and F. S. Pettit, *J. Electrochem. Soc.*, **118,** 1782 (1971).
31. G. R. Wallwork and A. Z. Hed, *Oxid. Met.*, **3,** 171 (1971).
32. C. A. Barrett and C. E. Lowell, *Oxid. Met.*, **11,** 199 (1977).
33. A. S. Tumarev and L. A. Panyushin, NASA TT F-13221, 1970; from *Izv. Vyssh. Uchebn. Zaved. Chern. Metall.*, **9,** 125 (1959).
34. C. Wagner, *Corr. Sci.*, **5,** 751 (1965).
35. B. H. Kear, F. S. Pettit, D. E. Fornwalt and L. P. Lemaire, *Oxid. Met.*, **3,** 557 (1971).
36. F. H. Stott and G. C. Wood, *Corr. Sci.*, **11,** 799 (1971).
37. R. Kosak and R. A. Rapp, in *Interamerican Conference on Materials Technology*, David Black (coord.), Centro Regional de Ayuda Technical, Mexico, 1972, pp. 813, 823.
38. J. L. Smialek and R. Gibala, *Met. Trans.*, **14A,** 2143 (1983).
39. I. A. Kvernes ad P. Kofstad, *Met. Trans.*, **3,** 1511 (1972).
40. G. J. Santoro, D. L. Deadmore, and C. E. Lowell, NASA TN D-6414, 1971.
41. J. L. Smialek and R. Gibala, in *High Temperature Corrosion*, R. Rapp (ed.), NACE, Houston, TX, 1983, p. 274.
42. K. P. Reddy and A. R. Cooper, *J. Am. Ceram. Soc.*, **65,** 634 (1982). Also K. P. Reddy, Ph.D. Thesis, Case Western Reserve University, May 1979.
43. J. D. Cawley, J. W. Halloran, and A. R. Cooper, NASA TM-83622, June 1984.
44. T. A. Ramanarayanan, M. Raghavan, and R. Petkovic-Luton, *J. Electrochem. Soc.*, **131,** 923 (1984).
45. A. E. Paladino and W. D. Kingery, *J. Chem. Phys.*, **37,** 957 (1962).
46. E. W. A. Young and J. H. W. deWit, *Sol. St. Ion.*, **16,** 39 (1985).
47. K. P. R. Reddy, J. L. Smialek, and A. R. Cooper, *Oxid. Met.*, **17,** 420 (1982).
48. G. C. Rybicki and J. L. Smialek, *Electrochem. Soc.*, Extended Abstracts, 1984 Spring Meeting (1984).
49. J. K. Doychak, T. E. Mitchell, and J. L. Smialek, *Mat. Res. Soc. Symp. Proc.*, **39,** 475 (1985).
50. J. K. Doychak, J. L. Smialek, and T. E. Mitchell, *Int. Cong. Met. Corr. Proc.*, **1,** 35 (1984).
51. J. L. Smialek and B. C. Buzek, *Bull. Am. Ceram. Soc.*, **58,** 144 (1979).
52. I. M. Allam, D. P. Whittle, and J. Stringer, *Oxid. Met.*, **12,** 35 (1978).
53. A. S. Khan, C. E. Lowell, and C. A. Barrett, *J. Electrochem. Soc.*, **127,** 670 (1980).
54. C. A. Barrett, A. S. Khan, and C. E. Lowell, *J. Electrochem. Soc.*, **128,** 25 (1981).
55. J. C. Pivin et. al., *Corr. Sci.*, **20,** 351 (1980).

56. F. A. Golightly, F. H. Stott, and G. C. Wood, *Oxid. Met.*, **10,** 163 (1976).
57. F. H. Stott, F. A. Golightly, and G. C. Wood, *Corr. Sci.*, **19,** 889 (1979).
58. F. H. Stott, G. C. Wood, and F. A. Golightly, *Corr. Sci.*, **19,** 869 (1979).
59. J. K. Tien and F. S. Pettit, *Met. Trans.*, **3,** 1587 (1972).
60. J. K. Kuenzly and D. L. Douglass, *Oxid. Met.*, **8,** 139 (1974).
61. C. S. Giggins and F. S. Pettit, ARL 75-0234, Aeronautical Research Laboratory, Dayton, OH, Final Report, June 1975.
62. E. Bullock, C. Lea, and M. McLean, *Met. Sci.*, **13,** 373 (June 1979).
63. J. H. Davidson et. al., in *Petten International Conference Proceedings*, The Metals Society, London, 1980, p. 209.
64. D. P. Whittle and J. Stringer, *Phil. Trans. Roy. Soc. Lond.*, **A295,** 305 (1980).
65. A. W. Funkenbusch, J. G. Smeggil, and N. S. Bornstein, *Met. Trans.*, **16A** 1164 (1985).
66. J. G. Smeggil, A. W. Funkenbusch, and N. S. Bornstein, *Met. Trans.* **17A,** 923 (1986).
67. K. L. Luthra and C. L. Briant, *Electrochem. Soc.*, Extended Abstracts, 1984 Spring Meeting, 1984, p. 26.
68. J. L. Smialek and R. L. Browning, NASA TM-87168, 1985. Also in *Electrochemistry Society, High Temperature Chemistry III Proceedings*, 1986, p. 258.
69. R. P. Messmer and C. L. Briant, *Acta Metall.*, **30,** 457 (1982).
70. J. G. Smeggil, Proc. 3rd. Corrosion/Erosion Materials Conf., A. Levy (ed.), NACE, Houston, TX, 1986.
71. J. L. Smialek, *Met. Trans.*, **18A,** 164 (1987).
72. C. E. Lowell, *Oxid. Met.*, **7,** 95 (1973).
73. D. L. Douglass and J. S. Armijo, *Oxid. Met.*, **2,** 207 (1970).
74. G. N. Irving, J. Stringer, and D. P. Whittle, *Oxid. Met.*, **8,** 393 (1974).
75. P. Tomaszewicz and G. R. Wallwork, in *High Temperature Corrosion*, R. A. Rapp)(ed.), NACE, Houston, TX, 1983, p. 258.
76. P. R. S. Jackson and G. R. Wallwork, *Oxid. Met.*, **21,** 135 (1984).
77. H. Nagai and M. Okabayashi, *Trans. Jap. Inst. Met.*, **22,** 691 (1981).
78. K. S. Chiang, Ph.D. Thesis, University of Pittsburgh, Pittsburgh, PA, 1980.
79. P. Elliot and A. F. Hampton, *Oxid. Met.*, **14,** 449 (1980).
80. G. M. Ecer and G. H. Meier, in *Properties of High Temperture Alloys*, Z. A. Foroulis and F. S. Pettit (eds.), The Electrochemical Society, Princeton, NJ, 1977, p. 279.
81. C. E. Lowell and G. J. Santoro, NASA TN D-6838, 1972.
82. S. W. Yang, *Oxid. Met.*, **15,** 375 (1981).
83. G. H. Meier and F. S. Pettit, unpublished research, 1986.
84. A. Kumar and D. L. Douglass, *Oxid. Met.*, **10,** 1 (1976).
85. R. V. Miner and C. E. Lowell, NASA TN D-7989, 1975.
86. R. V. Miner, *Met. Trans.*, **8A,** 1949 (1977).
87. H. W. Grunling and R. Bauer, *Thin Solid Films*, **95,** 3 (1982).
88. E. Fitzer and J. Schlichting, in *High Temperature Corrosion*, R. A. Rapp (ed.), NACE, Houston, TX, 1983, p. 604.
89. F. S. Pettit and G. H. Meier, in *Refractory Alloying Elements in Superalloys*, in J. K. Tien and S. Reichman (eds.), ASM, Metals Park, OH, 1984, p. 165.
90. S. T. Wlodek, *Trans. TMS-AIME*, **230,** 1078 (1964).
91. S. T. Wlodek, *Trans. TMS-AIME*, **230,** 177 (1964).
92. G. E. Wasielewski, AFML-TR-67-30, January 1967.
93. S. K. Rhee and A. R. Spencer, *Met. Trans.*, **1,** 2021 (1970).
94. S. K. Rhee and A. R. Spencer, *J. Electrochem. Soc.*, **119,** 396 (1972).
95. S. K. Rhee and A. R. Spencer, *Oxid. Met.*, **7,** 71 (1974).
96. S. K. Rhee and A. R. Spencer, *Oxid. Met.*, **8,** 11 (1974).
97. C. A. Barrett, G. J. Santoro, and C. E. Lowell, NASA TN-D-7484, 1973.
98. R. G. Garlick and C. E. Lowell, NASA TM X-2796, 1973.
99. C. E. Lowell and H. B. Probst, NASA TN D-7705, 1974.

100. G. C. Fryburg, F. J. Kohl, and C. A. Stearns, NASA TN-D-8388, 1977.
101. S. R. Smith, W. J. Carter, G. D. Mateescu, F. J. Kohl, C. Fryburg, and C. A. Stearns, *Oxid. Met.*, **14,** 415 (1980).
102. C. A. Barrett, R. V. Miner, and D. R. Hull, *Oxid. Met.*, **516,** 255 (1983).
103. C. A. Barrett, NASA TM-83784, 1984.
104. J. L. Smialek and C. A. Barrett, unpublished research, 1986.
105. C. A. Barrett, R. G. Garlick, and C. E. Lowell, NASA TM-83865, 1984.
106. C. A. Barrett, NASA TM 87297, 1986.